Mechanical bistability of the mesoderm epithelium facilitates mesoderm invagination during *Drosophila* gastrulation

Hanqing Guo[1], Michael Swan[2] and Bing He[1]*

1. Department of Biological Sciences, Dartmouth College, Hanover, NH

2. Department of Molecular Biology, Princeton University, Princeton, NJ

*Correspondence: Bing.He@dartmouth.edu

Abstract

Apical constriction driven by non-muscle myosin II ("myosin") provides a well-conserved mechanism to mediate epithelial folding. It remains unclear how contractile forces near the apical surface of a cell sheet drive out-of-the-plane bending of the sheet and whether myosin contractility is required throughout folding. By optogenetic-mediated acute inhibition of myosin, we find that during *Drosophila* mesoderm invagination, myosin contractility is critical to prevent tissue relaxation during the early, "priming" stage of folding but is dispensable for the actual folding step after the tissue passes through a stereotyped transitional configuration. The binary response suggests that the mesoderm is mechanically bistable during gastrulation. Combined modeling analysis and experimental measurements suggest that the observed mechanical bistability may arise from apicobasal shrinkage of the surrounding ectoderm, which promotes mesoderm invagination by facilitating a buckling transition. Our results suggest that *Drosophila* mesoderm invagination requires a joint action of local myosin contractility and mechanical bistability of the epithelium to trigger epithelial buckling.

Introduction

Contractile forces generated by actin and myosin ("actomyosin") networks are widely employed in embryogenesis to drive cell motility and cell shape change that pattern epithelial tissues (Martin and Goldstein, 2014; Munjal and Lecuit, 2014). During epithelial folding mediated by apical constriction, the actomyosin network in epithelial cells constricts cell apices, which leads to bending of the cell sheet (Sawyer et al., 2010). It remains unclear how "in-plane" contractile forces generated at the apical surface drives "out-of-the-plane" folding of the tissue. The invagination of the presumptive mesoderm during *Drosophila* gastrulation is a well-characterized epithelial folding process mediated by apical constriction (reviewed in Gilmour et al., 2017; Martin, 2020; Gheisari et al., 2020). During gastrulation, ventrally localized mesoderm precursor cells constrict their cell apices and become internalized into a ventral furrow. The folding process occurs in two steps (Leptin and Grunewald, 1990; Sweeton et al., 1991). During the first 10 – 12 minutes, the ventral cells undergo apical constriction and elongate in the apical-basal direction, while the cell apices remain near the surface of the embryo ("the lengthening phase"). In the next 6 – 8 minutes, the ventral cells rapidly internalize as they shorten back to a wedge-like morphology ("the shortening phase") (Figure 1a). Ventral furrow formation is controlled by the dorsal-ventral patterning system. The maternally deposited morphogen Dorsal controls the expression of two transcription factors, Twist and Snail, in the presumptive mesoderm. Twist and Snail in turn causes myosin activation at the apical pole of ventral mesodermal cells through a sequential action of G-protein coupled receptor (GPCR) signaling (Leptin, 1991; Parks and Wieschaus, 1991; Costa et al., 1994; Kolsch et al., 2007; Manning et al., 2013; Kerridge et al., 2016) and RhoGEF2-Rho1-Rho associated kinase (Rok) pathway (Barrett et al., 1997; Hacker and Perrimon, 1998; Nikolaidou and Barrett, 2004; Dawes-Hoang et

al., 2005; Martin et al., 2009; Mason et al., 2013). Activated myosin forms a supracellular actomyosin network across the apical surface of the prospective mesoderm and drives the constriction of cell apices (Martin et al., 2010, 2009; Martin and Goldstein, 2014).

The essential role of apical constriction in ventral furrow formation has been well demonstrated. Genetic mutations or pharmacological treatments that inhibit myosin activity disrupt apical constriction and result in failure in ventral furrow formation (reviewed in Gheisari et al., 2020; Martin, 2020). Biophysical studies show that cell shape change occurred during the lengthening phase is a direct, viscous response of the tissue interior to apical constriction (Gelbart et al., 2012; He et al., 2014). However, accumulating evidence suggests that apical constriction does not directly drive invagination during the shortening phase. First, it has been observed that the maximal rate of apical constriction (or cell lengthening) and the maximal rate of tissue invagination occur at distinct times (Polyakov et al., 2014; Rauzi et al., 2015). Second, it has been previously proposed, and more recently experimentally demonstrated, that myosin accumulated at the lateral membranes of constricting cells ('lateral myosin') facilitates furrow invagination by exerting tension along the apical-basal axis of the cell (Brodland et al., 2010; Conte et al., 2012; Gracia et al., 2019; John and Rauzi, 2021). Finally, a number of computational models predict that mesoderm invagination requires additional mechanical input from outside of the mesoderm, such as "pushing" forces from the surrounding ectodermal tissue (Munoz et al., 2007; Conte et al., 2009; Allena et al., 2010; Brodland et al., 2010). These models are in line with the finding that blocking the movement of the lateral ectoderm by laser cauterization inhibits mesoderm invagination (Rauzi et al., 2015). A similar disruption of ventral furrow formation can also be achieved by increasing actomyosin contractility in the lateral

ectoderm (Perez-Mockus et al., 2017). While these pioneer studies highlight the importance of cross-tissue coordination during mesoderm invagination, the actual mechanical mechanism that drives the folding of the mesodermal epithelium and the potential role of the surrounding ectodermal tissue remain to be elucidated.

In this study, we investigate the mechanics of ventral furrow formation by asking whether actomyosin contractility is required throughout the folding process. By developing an optogenetic tool to acutely inhibit actomyosin activity, we find that the mesoderm primordium is mechanically bistable during gastrulation. Using computer simulation, we show that combining apical constriction in the mesoderm and in-plane compression from the neighboring ectoderm is sufficient to recapitulate the bistable characteristic of the mesoderm. Finally, we show evidence that the lateral ectoderm undergoes apicobasal shortening/shrinkage during gastrulation, a process that may generate in-plane compression. The ectodermal shortening process, as well as the associated ventrally directed movement of the ectoderm, is independent of mesoderm invagination. Taken together, we propose that mechanical bistability in the mesoderm enabled by the surrounding ectoderm functions together with apical constriction to facilitate mesoderm invagination.

Results

Plasma membrane recruitment of Rho1DN results in rapid loss of apical myosin and F-actin network

In order to acutely inhibit myosin activity in live embryos (Figure 1a), we generated an optogenetic tool, "Opto-Rho1DN", to inhibit Rho1 through light-dependent plasma membrane recruitment of a dominant negative form of Rho1 (Rho1DN). Like other Rho GTPases, Rho1 cycles between an active, GTP-bound state and an inactive, GDP-bound state (Etienne-Manneville and Hall, 2002). Rho1DN bears a T19N mutation, which abolishes the ability of the mutant protein to exchange GDP for GTP and thereby locks the protein in the inactive state (Barrett et al., 1997). A second mutation in Rho1DN, C189Y, abolishes its naive membrane targeting signal (Sebti and Der, 2003; Roberts et al., 2008). When Rho1DN is recruited to the plasma membrane, it binds to and sequesters Rho1 GEFs, thereby preventing activation of endogenous Rho1 as well as Rho1-Rok-mediated activation of myosin (Barrett et al., 1997; Feig and Cooper, 1988).

Opto-Rho1DN is based on the CRY2-CIB light-sensitive dimerization system (Liu et al., 2008; Kennedy et al., 2010; Guglielmi et al., 2015) (Figure 1b). The tool contains two components: a GFP-tagged N-terminal of CIB1 protein (CIBN) anchored at the cytoplasmic leaflet of the plasma membrane (CIBN-pmGFP) (Guglielmi et al., 2015), and a fusion protein with Rho1DN, an mCherry tag, and a blue light-reactive protein Cryptochrome 2 (CRY2-Rho1DN). CRY2-Rho1DN remained in the cytoplasm when the sample was kept in dark or imaged with a yellow-green (561-nm) laser (Figure 1c, T = 0). Upon blue (488-nm) laser stimulation, CRY2 undergoes a conformational change and binds to CIBN (Kennedy et al., 2010; Liu et al., 2008), resulting in

rapid recruitment of CRY2-Rho1DN to the plasma membrane (Figure 1c, d; Figure 1-video 1). The average time for half-maximal membrane recruitment of CRY2-Rho1DN is 4 seconds (3.9 ± 2.8 sec, mean ± s.d., n = 5 embryos). Embryos expressing CIBN-pmGFP and CRY2-Rho1DN developed normally in a dark environment and could hatch (100%, n = 63 embryos). In contrast, most embryos (>85%, n = 70 embryos) kept in ambient room light failed to hatch, reflecting the essential role of Rho1 in *Drosophila* embryogenesis (Barrett et al., 1997; Magie et al., 1999; Johndrow et al., 2004).

The effectiveness of Opto-Rho1DN on myosin inactivation was validated by stimulating embryos during apical constriction, which resulted in diminishing of apical myosin signal within 60 seconds (Figure 1e, f; Figure 1-video 2). Rapid disappearance of cortical myosin upon Rho1 inhibition is consistent with the notion that Rho1 and myosin cycle quickly through active and inactive statues due to the activity of GTPase activating proteins (GAPs) for Rho1 and myosin light chain phosphatases, respectively (Munjal et al., 2015; Coravos and Martin, 2016). Our data also provide direct evidence that sustained myosin activity during ventral furrow formation requires persistent activation of Rho1.

In addition to myosin, we found that acute Rho1 inhibition also affects cortical F-actin networks during apical constriction, presumably through inactivation of the Rho1 effector formin Diaphanous (Johndrow et al., 2004; Homem and Peifer, 2008; Mason et al., 2013; Coravos and Martin, 2016). In unstimulated embryo, F-actin is enriched at the apical domain of the constricting cells (Figure 2a, red arrowhead and cyan arrows) and along the lateral membrane in both constricting and non-constricting cells (Figure 2a, yellow arrows and magenta arrows).

Apical F-actin disappeared within 1.2 minutes after Opto-Rho1DN stimulation (Figure 2b). Lateral F-actin in the constricting cells was not immediately affected and only appeared to diminish 4 minutes after stimulation (Figure 2b). In contrast, lateral F-actin in the ectodermal cells was not significantly affected (Figure 2b). Taken together, our results indicate that Opto-Rho1DN is an effective tool for spatial- and temporal-confined inactivation of apical actomyosin contractility through simultaneous myosin inactivation and actin disassembly.

Consistent with the actomyosin phenotype, Opto-Rho1DN stimulation before or during apical constriction resulted in prevention or reversal of apical constriction, respectively (Figure 1 – figure supplement 1). In addition, Opto-Rho1DN stimulation resulted in an immediate loss of cortical tension at the ventral surface of the embryo during apical constriction (Figure 3), in accordance with previous finding that the increase in tissue tension in the ventral mesodermal region during apical constriction is due to activation of apical myosin contractility and integration of contractile forces across the constriction domain (Martin et al., 2010). Finally, by stimulating the embryo within a specific region of interest, we showed that membrane recruitment of CRY2-Rho1DN and inhibition of apical constriction are restricted to cells within the stimulated region (Figure 1g, Figure 1 – figure supplement 1c, d).

Acute inhibition of myosin contractility reveals mechanical bistability of the mesoderm during gastrulation

Using Opto-Rho1DN, we determined the role of actomyosin contractility at different stages of ventral furrow formation. We first obtained non-stimulated control movies by imaging embryos bearing Opto-Rho1DN on a multiphoton microscope using a 1040-nm pulsed laser, which

excites mCherry but does not stimulate CRY2 (Guglielmi et al., 2015). Without stimulation, the embryos underwent normal ventral furrow formation (Figure 4a). The transition from the lengthening phase to the shortening phase ($T_{L\text{-}S\ trans}$) occurred around ten minutes after the onset of gastrulation (9.3 ± 1.6 minutes, mean ± s.d., n = 10 embryos), which was similar to the wildtype embryos (8.9 ± 0.8 minutes, mean ± s.d., n = 6 embryos) (Figure 4 – figure supplement 1a-c). This transition was characterized by a rapid inward movement of the apically constricted cells and could be readily appreciated by the time evolution of distance between the cell apices and the vitelline membrane of the eggshell (invagination depth "D", Figure 4 – figure supplement 1d).

Next, we examined the effect of Opto-Rho1DN stimulation on furrow invagination (Figure 4b; Figure 4 – figure supplement 1e; Methods). Measuring the rate of furrow invagination (dD/dt) immediately after stimulation revealed three types of tissue responses to stimulation (Figure 4a, b; Figure 4 – figure supplement 1f, g; Figure 4-video 1). For most embryos that were stimulated before T = 7 minutes ("Early Group" embryos), the constricting cells relaxed immediately. The initial apical indentation disappeared ($dD/dt < 0$). The flanking, non-constricting cells, which were previously apically stretched by neighboring constricting cells, shrunk back, indicating that the apical cell cortex was elastic (Figure 4 – figure supplement 2a, b). In contrast, for most embryos that were stimulated after T = 7 minutes ("Late Group" embryos), furrow invagination proceeded at a normal rate and dD/dt remained positive. Finally, some embryos stimulated around T = 7 minutes (6.5 ± 1.4 minutes, mean ± s.d., n = 4 embryos; "Mid Group" embryos) displayed an intermediate phenotype, where ventral furrow invagination paused for around five minutes (4.7 ± 0.5 minutes; $dD/dt \approx 0$) before invagination resumed. We confirmed that there

was no residual apical myosin in Late Group embryos upon stimulation (Figure 4 – figure supplement 3a). Furthermore, lateral myosin, which has been shown to facilitate furrow invagination (Gracia et al., 2019; John and Rauzi, 2021), also quickly disappeared after stimulation (Figure 4 – figure supplement 3b, c). Overall, furrow invagination in Late Group embryos is not due to myosin activities at the apical or lateral cortices of the mesodermal cells. Together, these results indicate that actomyosin contractility is required in the early but not the late phase of furrow formation. The narrow time window when Mid Group embryos were stimulated defined the "transition phase" for sensitivity to myosin inhibition (T_{trans}), which is immediately before $T_{L\text{-}S\ trans}$ (Figure 4c).

While all Early Group embryos showed tissue relaxation after stimulation, 5 out of 8 of them were able to invaginate after a prolonged delay (Figure 4b; Figure 4 – figure supplement 2c-f). The invagination was associated with modest myosin reaccumulation at the cell apices that occurred approximately ten minutes after the initial stimulation (Figure 4 – figure supplement 2e-f). It is unclear why apical myosin sometimes reoccurred in the presence of persistent membrane localization of CRY2-Rho1DN. Nevertheless, the completion of furrow invagination when apical constriction is partially impaired is consistent with previous genetic studies and suggests that invagination is facilitated by additional mechanical input (Costa et al., 1994; Parks and Wieschaus, 1991).

Because the response of ventral furrow formation to myosin inhibition appears to be binary, we sought to identify morphological features of the progressing furrow that associate with T_{trans}. Hence, we examined the relationship between D immediately after stimulation ("D_s") and the

extent by which furrow invagination is affected (assessed by the delay time in furrow invagination, T_{delay}, see Methods). We found that for stimulated embryos, T_{delay} was ultrasensitive to D_s, with a steep transition at around 6 μm (Figure 4d). When D_s was above the threshold, T_{delay} was close to 0. When D_s was below the threshold, T_{delay} increased to ten minutes (9.4 ± 1.4 minutes, mean ± s.d., n = 5 Early Group embryos) or longer (fail to invaginate, n = 3 Early Group embryos). Therefore, the response to acute myosin inhibition can be well predicted by the tissue morphology associated with the stage of furrow progression.

The binary response of the embryo to acute myosin inhibition suggests that the mesoderm during gastrulation is mechanically bistable and has two stable equilibrium states: the initial, pre-constricted conformation and the final, fully invaginated conformation (Figure 4e). Energy input from actomyosin-mediated apical constriction drives the transition from the initial state to an intermediate state (T_{trans}), which has the propensity to transition into the final state without further requirement of actomyosin contractility. If myosin is inhibited before T_{trans}, the furrow would relax back to the initial state. In contrast, if myosin is inhibited after T_{trans}, the furrow would continue to invaginate without pause (Figure 4e).

Analysis of three-dimensional cell shape change after Opto-Rho1DN stimulation

To gain further insights of how cells respond to rapid myosin loss after Rho1 inhibition, we performed three-dimensional cell reconstruction using ilastik (Berg et al., 2019). For each embryo, we examined a single row of cells (cell 1-11) along the medial-lateral axis that include the ventral mesodermal cells (~cell 1 – 6, "constricting cells"), the lateral mesodermal cells (~cell 7 – 9, "non-constricting flanking cells"), and presumably some ectodermal cells (~cell 10

– 11) (Figure 5a and 5f). Our analysis covered timepoints with most notable cell shape changes after stimulation (0, 2.2 and 4.4 minutes for Early Group embryos, and 0, 1.1 and 2.2 minutes for Late Group embryos). Shorter time windows were used for Late group embryos because of the rapid furrow invagination despite the inhibition of actomyosin contractility.

As expected, in Early Group embryos, there was a prompt apical area relaxation in the constricting cells and an accompanying apical area reduction in the flanking cells following stimulation (See Figure 5b for a cartoon depiction). A number of features were observed in Early Group embryos. First, there was no substantial cell volume change (± 5%, Figure 5 – figure supplement 1), similar to the observation for normal ventral furrow formation (Gelbart et al., 2012; Polyakov et al., 2014). Second, the flanking cells that were most apically stretched before stimulation underwent most prominent apical area reduction, which is anticipated (comparing cell 7, 8 and 9, Figure 5c). Surprisingly, the extent of apical relaxation in the constriction domain was not uniform. In general, cells located at the side of the constriction domain ("side constricting cells", cell 4 – 6) relaxed more than those located closer to the ventral midline ("mid constricting cells", cell 1 – 3) (Figure 5c). The lower degree of apical relaxation in the mid-constriction cells was accompanied with less prominent "reversal of lengthening" (Figure 5d, see Figure 5b for a cartoon depiction). Finally, the alteration in apical cell area was associated with changes in cell curvature along the apical-basal axis. Before stimulation, the flanking cells and the side constricting cells were all tilted, with their apical side bending towards the ventral midline (e.g., yellow and orange cells in Figure 5a). After stimulation, the cells straightened up and partially restored their initial, columnar cell shape. This cell shape change is associated with a reduction in the apical-basal cell length and lateral cell area (Figure 5b, d, e; Figure 5 – figure

supplement 1). The ectodermal cells also showed some unbending, but their shape changes were in general moderate (Figure 5, cell 10 – 11).

Interestingly, despite the drastic tissue level difference between Early and Late groups of embryos, several trends we observed in Early group was also present in Late group, such as the conservation of cell volume (Figure 5 – figure supplement 1), the straighten-up of some (but not all) flanking cells (e.g. cell 9 in Figure 5j), and the uneven pattern of apical relaxation in the constriction domain (Figure 5h). Despite these similarities, Late Group embryos displayed several prominent features that were distinct from Early Group embryos (see Figure 5b and 5g for a cartoon depiction). First, the mid constricting cells barely showed any apical relaxation and underwent rapid cell shortening after stimulation (Figure 5h and 5i, cell 1 – 3), which were not observed in Early Group embryos but rather resembled the normal cell shortening process (Polyakov et al., 2014). Second, despite undergoing apical relaxation, the side constricting cells bent further towards the ventral midline instead of straightening up as their counterparts in Early Group embryos (Figure 5j, cell 4 – 6). The behavior of the middle and side constricting cells in Late Group embryos elucidates the cellular basis for the continued deepening of the furrow after Opto-Rho1DN stimulation and explains the tissue level difference between Early and Late Group embryos. Importantly, the observed cell shape change and tissue invagination in Late Group embryos occurred in the absence of actomyosin contractility, suggesting the presence of additional mechanical contributions.

Mechanical bistability of the mesoderm during gastrulation can arise from ectoderm-derived compressive stresses

What mechanism may account for mechanical bistability in the folding process? Previous biophysical studies demonstrate that the embryonic epithelium in early *Drosophila* embryos can display an elastic response with a decay timescale of at least four minutes (Doubrovinski et al., 2017). The bistable characteristic of the mesoderm is reminiscent of a compressed elastic beam undergoing snap-through buckling facilitated by a transverse "indentation force" (Figure 6b; Jin Qiu et al., 2004). Based on this analogy, we hypothesized that mesoderm invagination is mediated through tissue buckling enabled by in-plane compressive stresses. We tested this hypothesis by implementing compressive stresses from the ectoderm in a previously published 2-dimensional vertex model for ventral furrow formation (Polyakov et al., 2014; Figure 6a; Methods). In this model, the sole energy input is apical constriction of the ventral cells, whereas the apical, lateral, and basal cortex of cells were represented by elastic springs that resist deformation. By allowing the model to transition through a series of intermediate states governed by a step-wise reduction of basal cell rigidity, the resulting cell shape changes recapitulate the lengthening-shortening dynamics of the constricting cells in the actual embryos (Polyakov et al., 2014; Methods).

Using this model, we simulated the effect of acute myosin loss by removing the apical contractile forces at different intermediate states of the model (Methods). Remarkably, in the presence of ectodermal compression, the model recapitulated the binary response to loss of apical constriction as observed experimentally (Figure 6c). In particular, the transitional state of the tissue revealed in the simulation is nearly identical to that identified in our optogenetic experiments. As a control, in the absence of ectodermal compression, the model always returned to its initial configuration regardless of the stage when apical constriction was eliminated (Figure

6c). Therefore, buckling of an elastic cell sheet can well reproduce the bistable characteristics of the mesoderm observed in real embryos. Our model also predicts that the presence of ectodermal compression could compensate for partial impairment of apical constriction (Figure 6d), which explains why some Early Group embryos could still invaginate when myosin activity was greatly downregulated.

Interestingly, our simulation predicts that for embryos stimulated after T_{trans}, the ventral furrow at the final invaginated state would be narrower with fewer cells being incorporated into the furrow compared to control embryos. Our observation in Late Group embryos well matched this prediction (Figure 6c; Figure 6 – figure supplement 1a, b). Consistent with our 3D analysis (Figure 5h), we found that stimulation in Late Group embryos induced a mild but noticeable alteration in tissue flow that indicates the occurrence of apical relaxation in the constricted cells (Figure 6 – figure supplement 1c, d). These results suggest that maintaining actomyosin contractility after T_{trans} helps to prevent local relaxation of the apical membranes, thereby allowing more cells to be incorporated into the furrow. This "late" function of actomyosin contractility is dispensable for furrow invagination per se but is important for the complete internalization of the prospective mesoderm.

Presence of myosin-independent cell shortening force in the constriction domain is important for the vertex model to recapitulate the observed binary response

In the vertex model described above, shortening of the constricting cells is mediated by passive elastic restoration forces generated in these cells as their lateral edges are stretched during cell lengthening (Polyakov et al., 2014). This passive elastic force is not affected by in silico myosin

inactivation. However, our experiments show that Opto-Rho1DN stimulation results in rapid diminishing of lateral myosin in the constricting cells, suggesting that Rho1 inhibition may weaken the shortening forces in these cells (Gracia et al., 2019; John and Rauzi, 2021). To account for this effect, we implemented active lateral constriction forces in the ventral cells. In such a scenario, the active and passive lateral forces worked in combination to mediate ventral cell shortening, but only the active force was sensitive to myosin inactivation (Methods). The active and passive lateral forces were given by $K_{L_active}l$ and $K_{L_passive}(l - l_0)$, respectively, where l and l_0 were the current and the resting length of the lateral edge, respectively. As expected, the addition of the active lateral force allows us to reduce the passive lateral force while still generate furrows with normal morphology (Figure 7a, comparing column K_{L_active} = 0 with column K_{L_active} = 2). The implementation of myosin-dependent active lateral forces allowed us to examine how the binary response would be influenced if myosin inactivation weakens the cell shortening forces in the mesoderm.

We performed the tests under the conditions where the model generates normal furrow morphology (green shaded region in Figure 7a, $K_{L_passive} = 20$ while K_{L_active} ranges from 0 to 2, or $K_{L_active} = 2$ while $K_{L_passive}$ ranges from 0.002 to 20). When $K_{L_passive} = 20$, changing K_{L_active} has little impact on the response of the model to stimulation (Figure7b). When $K_{L_active} = 2$, changing $K_{L_passive}$ did not affect the binary tissue response per se but influenced the final morphology after stimulation (Figure 7c). When the passive lateral force was relatively high ($K_{L_passive} = 20$), the model displayed normal binary response with realistic final furrow morphologies. Lowering the passive lateral force by a factor of ten ($K_{L_passive} = 2$) did not change the tissue response aside from a mild reduction of the invagination depth "D" (from 61

μm to 51 μm) in Late Group embryos. Strikingly, further lowering $K_{L_passive}$ to 0.2 resulted in a very shallow furrow and abnormal constricting cell morphology in Late Group embryos (D = 30 μm). Together, these results demonstrate that the binary response of the model to myosin inhibition still exists when the cell shortening forces in the mesoderm become sensitive to myosin inhibition. However, a minimal level of myosin-independent lateral elastic force ($K_{L_passive} > 0.2$) is required for the model to generate realistic final furrow morphology in Late Group embryos. Interestingly, we found that lateral actin in the constricting cells persisted for several minutes after Opto-Rho1DN stimulation (Figure 2b, yellow arrows), which might provide the lateral elasticity described in our model.

The lateral ectoderm undergoes apical-basal shortening during gastrulation independently of ventral furrow formation

The presence of compressive stresses in the ectoderm during gastrulation has not been previously reported. No cell division happens in the embryo during ventral furrow formation (Foe and Alberts, 1983; Edgar et al., 1994), thereby excluding a role for cell proliferation in generating compressive stresses as seen in many other tissues (Nelson, 2016). Interestingly, it has been reported that ectodermal cells undergo apical-basal shortening during gastrulation (Brodland et al., 2010). In theory, this cell shape change could generate compressive stresses in the planar direction if the cell volume remains conserved. To further investigate the extent of ectodermal shortening during gastrulation, we performed 3D tissue volume measurement ("Vol_{ec}") in the lateral ectodermal region of wildtype embryos ("ROI": 60-120 degrees away from the ventral midline and 75 μm long along the AP axis; Figure 8a). We focused our analysis on the lateral ectodermal region since a previous study shows that the dorsal ectoderm does not significantly

contribute to ventral furrow formation (Rauzi et al., 2015). We reasoned that if the ectodermal cells undergo apical-basal shortening, there should be a net volume outflux from the ROI, causing a reduction in Vol_{ec} (Figure 8a). Since cell shortening may not be uniform across the tissue, the change in Vol_{ec} provides a less noisy measure of the change in average tissue thickness. To measure Vol_{ec}, we performed 3D tissue segmentation without segmenting individual cells (Methods).

This analysis led to the following observations. First, Vol_{ec} increased during the first ten minutes of ventral furrow formation (Figure 8c). This observation is consistent with the previous measurement of ectodermal cell length during gastrulation (Brodland et al., 2010). Second, in all cases examined, Vol_{ec} started to decrease approximately halfway through ventral furrow formation, but the exact time of this transition varied between embryos (11.1 ± 2.3 min, mean ± s.d., n = 3 embryos; Figure 8f, arrowheads). Finally, the percent reduction in Vol_{ec} from the peak volume to that at the end of ventral furrow formation ranged between 4 – 8%. These observations are consistent with an independent 2D measurement of the cross-section area (as a proxy for tissue thickness) of a lateral ectodermal region that was between 60 and 90 degrees from the ventral midline (~ 6% reduction; Figure 8 – figure supplement 1).

The observed ectodermal shortening could be driven by an active mechanism that reduces cell length or could be a passive response to the pulling from ventral furrow. To distinguish these possibilities, we repeated the Vol_{ec} measurements in *snail* mutant embryos. As expected, ventral furrow failed to form in *snail* embryos (Figure 8g). Strikingly, the reduction of Vol_{ec} occurred at about the same time as in the wildtype. In addition, the rate of Vol_{ec} reduction was similar

between the wildtype and *snail* embryos, although the *snail* embryos on average had a smaller Vol_{ec} to start with (Figure 8d and f). This result indicates that pulling from ventral furrow cannot fully account for the apicobasal shrinkage of lateral ectoderm in the wildtype embryos and suggests the presence of ventral furrow-independent mechanism for ectodermal shortening.

In our vertex model, ectodermal compression was generated by letting all ectodermal cells shorten by 20% ($\Delta L = 20\%$; Methods), which was greater than the range measured in the actual embryos. We found that in our model, a minimum of 5 – 10% shortening in all 60 ectodermal cells is critical for generating the binary response (Figure 8 – figure supplement 2). A number of factors may account for the difference between the model and the actual embryo. For example, while an apicobasal shrinkage of the ectodermal cells can generate in-plane compression, the onset and the effect of this shrinkage may be underestimated by volume or length measurement if the cells are growing at the same time (Figure 8c, first 10 min). In addition, other morphogenetic processes happening during gastrulation might also contribute to the generation of tissue compression (Rauzi et al., 2015). While our model recapitulated the main cell morphological features during ventral furrow formation and correctly predicted the binary response to acute actomyosin inhibition, future research is needed to elucidate the mechanism and function of ectodermal shortening in gastrulation.

Ventrally directed movement of the lateral ectoderm still occurs when apical constriction in the mesoderm is inhibited

In theory, compression generated by ectodermal shortening should result in displacement of the ectodermal cells towards the ventral region regardless of whether mesoderm invagination occurs.

Previous studies have shown that ventral movement of the lateral ectoderm still occurs in mesoderm specification mutants that do not form ventral furrow (Rauzi et al., 2015). Our own observation in the *snail* mutant is also consistent with this result (Figure 8e). Interestingly, we found that in *snail* mutant embryos, cells moved towards both ventral and posterior sides as soon as ectodermal shortening began (Figure 8d). This is in sharp contrast to the wildtype embryos, where the onset of the posteriorly directed movement commenced 20 – 25 minutes later than the onset of Vol_{ec} reduction and ventrally directed movement (Figure 8c). The altered pattern of cell movement in *snail* embryos may be caused by a combined effect of ectodermal compression and lack of ventral furrow invagination (Figure 8f). In wildtype embryos, the compression promotes ventral furrow invagination, which in turn functions as a "sink" to facilitate (and thereby bias) the movement of the ectoderm in the ventral direction. However, since the *snail* mutant embryos do not form ventral furrow, an increase in ectodermal compression induces tissue movement in a both A-P and D-V axis simultaneously, albeit slower.

So far, data from ours and others have shown that ventrally directed ectoderm movement still occurs without ventral furrow formation. It remains unclear, however, whether this decoupling of tissue movement can be observed without altering cell fate specification. Our optogenetic approach provided an opportunity for us to test this. First, we examined the ectodermal movement in the Early Group embryos immediately after stimulation. Our measurements confirmed the "reverse" movement of the ventral cells during tissue relaxation and demonstrated that during the same time period the lateral ectoderm moved in the opposite direction, towards the ventral midline (Figure 9a-9e). Second, we inhibited Rho1 at the onset of apical constriction to mimic the ventral furrow phenotype of the *snail* mutants, but without changing mesodermal

cell fate (Figure 9f-9g). Despite the lack of apical constriction, we observed ventrally directed ectodermal movement similar to that in the *snail* mutants (Figure 9f). These results indicate that the ventrally directed lateral ectoderm movement can occur independent of ventral furrow formation when cell fate specification is expected to be normal. Taken together, our observations suggest that ectodermal shortening may serve as an independent mechanical input that facilitates mesoderm invagination by promoting mechanical bistability in the mesoderm.

Discussion

In this work, we developed an optogenetic tool, Opto-Rho1DN, to acutely inhibit actomyosin contractility in developing embryos. Using this tool, we discovered that while actomyosin-mediated active cell deformation is critical for mesoderm invagination, it is dispensable during the subsequent rapid invagination step after a transitional stage (T_{trans}), when the initial apical constriction mediated "tissue priming" is completed. These observations demonstrate that the mesoderm is mechanically bistable during gastrulation, a mechanical status analogous to an elastic beam under compression. Using computer modeling, we further demonstrate that mechanical bistability in the mesoderm can arise from an apicobasal shrinkage of the ectoderm, which generates in-plane compression as the cell volume remains conserved. Finally, by measuring volume change in the lateral ectodermal region in both wildtype and *snail* mutant embryos, we show that apicobasal shrinkage of lateral ectoderm still occurs in the absence of ventral furrow formation and may thereby offer an independent mechanical input to facilitate mesoderm invagination. We propose that ventral furrow formation is mediated through a joint action of multiple mechanical inputs. Apical constriction drives initial indentation of ventral furrow, which primes the tissue for folding, whereas the subsequent rapid folding of the furrow is promoted by bistable characteristic of the mesoderm and by lateral myosin contractions in the constricting cells (Figure 9h). We further hypothesize that ectodermal compression induced by apical-basal cell shortening of the ectodermal cells induces mechanical bistability in the mesoderm, which in turn facilitates mesoderm invagination through a buckling-like mechanism (Figure 9h). Future experiments investigating the presence and potential function of ectodermal compression would be key to testing these hypotheses.

In principle, bending of a cell sheet can be achieved through two general mechanisms. In the first mechanism, an active cell deformation (e.g. apical constriction) that results in cell wedging can cause the tissue to acquire a folded configuration. In this case, the mechanism is tissue autonomous and does not necessarily require active mechanical contributions from neighboring tissues. In the second mechanism, bending of a cell sheet is prompted by an increase in the compressive stresses within the tissue (Mao and Baum, 2015). This mechanism is tissue non-autonomous and depends on the tissues surrounding the region where folding happens. The canonical model for apical constriction-mediated cell sheet folding emphasizes the role of active cell deformation in the constriction domain (Wolpert et al., 2015). A number of recent studies, however, have implicated additional mechanical contributions from outside of the constriction domain that can influence apical constriction-mediated tissue folding (Rauzi et al., 2015; Perez-Mockus et al., 2017). Our results further support this notion and suggest that ventral furrow formation involves both tissue autonomous and non-autonomous mechanisms. In such a scenario, the generation of ectodermal compression increases the buckling propensity of the epithelium, whereas the active cell shape change induced by apical constriction triggers buckling at a defined position. The requirement for this tissue level cooperation may explain the recent data showing that ectopic activation of Rho1 activity at different regions of cellular blastoderms in *Drosophila* results in different final furrow morphology (Rich et al., 2020).

Drosophila ventral furrow formation is a robust process in that it can still happen in various scenarios when apical constriction is weakened (Leptin and Grunewald, 1990; Parks and Wieschaus, 1991; Kolsch et al., 2007; Yevick et al., 2019). Recent studies have revealed that the supracellular actomyosin network is intrinsically robust, with build-in redundancies to secure

global connectivity of the network (Yevick et al., 2019). Mechanical bistability of the mesoderm enabled by ectodermal shortening provides an alternative, tissue-extrinsic mechanism that allows proper invagination of the mesoderm when actomyosin contractility in the mesodermal cells is impaired due to genetic and environmental variations.

Actomyosin contractility provides a common force generation mechanism in development. To date, the studies of tissue mechanics have been largely focused on the mechanisms that generate contractile forces that actively deform the tissues (Gilmour et al., 2017; Heisenberg and Bellaïche, 2013; Chanet and Martin, 2014). It remains less well understood how the "passive" mechanical status of the tissue influences the outcome of tissue deformation. The Opto-Rho1DN optogenetic tool developed in this work provides an effective approach to acutely disrupt the myosin-dependent force generation machinery, and therefore can help us begin to discern the role of "active" forces and "passive" mechanical properties in morphogenesis. Furthermore, our work provides an example for the cooperation between "local", tissue-autonomous active force production and "global", tissue-nonautonomous mechanical contribution in tissue morphogenesis. It will be interesting to explore whether such cooperation plays a role in other cell sheet folding processes and whether mechanisms other than apical constriction can be employed to trigger folding in a compressed cell sheet.

Materials and Methods

Key Resources Table				
Reagent type (species) or resource	**Designation**	**Source or reference**	**Identifiers**	**Additional information**
genetic reagent (*D. melanogaster*)	*Sqh-GFP*	Royou et al., 2002		
genetic reagent (*D. melanogaster*)	*Sqh-mCherry*	Martin et al., 2009		
genetic reagent (*D. melanogaster*)	*E-cadherin-GFP*	Oda and Tsukita, 2001		
genetic reagent (*D. melanogaster*)	*UASp-P4M-mCherry*	Chen and He, 2021		
genetic reagent (*D. melanogaster*)	*Utrophin-Venus*	Figard and Sokac, 2011		
genetic reagent (*D. melanogaster*)	*halo snail/CyO, Sqh-GFP*	Martin et al., 2009		
genetic reagent (*D. melanogaster*)	*UASp-CIBN-pm-GFP (II)*	Guglielmi et al., 2015		
genetic reagent (*D. melanogaster*)	*UASp-CIBN-pm (I)*	Guglielmi et al., 2015		
genetic reagent (*D. melanogaster*)	*UASp-CRY2-Rho1DN -mCherry (III)*	This study		See "Fly stocks and genetics" for details
genetic reagent (*D. melanogaster*)	*UASp-CIBN-pm-GFP; CRY2-Rho1DN*	This study		See "Fly stocks and genetics" for details

genetic reagent (*D. melanogaster*)	*UASp-CIBN-pm; CRY2-Rho1DN*	This study		See "Fly stocks and genetics" for details
genetic reagent (*D. melanogaster*)	*Maternal-Tubulin-Gal4 ("67")*	Hunter and Wieschaus, 2000		*Maternal-Tubulin-Gal4* on Chromosome II
genetic reagent (*D. melanogaster*)	*Maternal-Tubulin-Gal4 ("15")*	Hunter and Wieschaus, 2000		*Maternal-Tubulin-Gal4* on Chromosome III
genetic reagent (*D. melanogaster*)	*67; 15*	Hunter and Wieschaus, 2000		*Maternal-Tubulin-Gal4* on II & III
genetic reagent (*D. melanogaster*)	*67 Sqh-mCherry; 15 Sqh-GFP*	This study		See "Fly stocks and genetics" for details
genetic reagent (*D. melanogaster*)	*67 Sqh-mCherry; 15 E-cadherin-GFP*	This study		See "Fly stocks and genetics" for details
genetic reagent (*D. melanogaster*)	*67 Sqh-GFP; 15*	This study		See "Fly stocks and genetics" for details
genetic reagent (*D. melanogaster*)	*67 Sqh-GFP; 15 Sqh-GFP*	This study		See "Fly stocks and genetics" for details
genetic reagent (*D. melanogaster*)	*67 Sqh-mCherry; 15 Utrophin-Venus*	This study		See "Fly stocks and genetics" for details
genetic reagent (*D. melanogaster*)	*67 Sqh-GFP; 15 P4M-mCherry*	This study		See "Fly stocks and genetics" for details
recombinant DNA reagent	pTiger	S. Ferguson, State University of New York at Fredonia		Transformation vector containing the attB site and 14 upstream UAS sites

recombinant DNA reagent	pTiger-CRY2-mCherry-Rho1DN	This study		Transformation construct containing CRY2-mCherry-Rho1DN
software, algorithm	Matlab	MathWorks		https://www.mathworks.com/?s_tid=gn_logo RRID:SCR_001622
software, algorithm	FIJI	ImageJ		http://fiji.sc RRID:SCR_002285
software, algorithm	Embryo Development Geometry Explorer (EDGE)	Gelbart et al., 2012		https://github.com/mgelbart/embryo-development-geometry-explorer
software, algorithm	ilastik	Berg et al., 2019		https://www.ilastik.org/ RRID:SCR_015246

Generation of CRY2-Rho1DN construct

To generate the CRY2-mCherry-Rho1DN fusion gene, the Rho1 CDS bearing an ACT to AAT mutation and a TGC to TAC mutation (T19N and C189Y, respectively) was synthesized and inserted to the C-terminal end of pCRY2PHR-mCherryN1 (Addgene, deposited by Chandra Tucker) through Gibson assembly. A 12-aa flexible linker sequence (GGGGSGGGGSGG) was included between the mCherry and Rho1DN sequences. The resulting CRY2PHR-mCherry-Rho1N18Y189 fusion gene was subsequently inserted into pTiger, a transformation vector containing the attB site and 14 upstream UAS GAL4-binding sites (courtesy of S. Ferguson, State University of New York at Fredonia, Fredonia, NY, USA). The resulting pTiger-CRY2-mCherry-Rho1DN construct was sent to Genetic Services for integration into the attP2 site using the phiC31 integrase system (Groth et al., 2004).

Fly stocks and genetics

Fly lines containing the following fluorescent markers were used: *Sqh-GFP* (Royou et al., 2002), *Sqh-mCherry* (Martin et al., 2009), *E-cadherin-GFP* (Oda and Tsukita, 2001), *P4M-mCherry* (Chen and He, 2021) and *Utrophin-Venus* (Figard and Sokac, 2011). To generate *snail* mutant embryos, we used the *halo snail/CyO, Sqh-GFP* line (Martin et al., 2009).

Fly lines containing *CIBN-pm-GFP (II), CIBN-pm (I)* (Guglielmi et al., 2015) or *CRY2-Rho1DN (III)* (this study, note that *CRY2-Rho1DN* also contains the *mCherry* tag) were used to generate the following stocks: *CIBN-pm-GFP; CRY2-Rho1DN* and *CIBN-pm; CRY2-Rho1DN*. To generate embryos containing maternally deposited CIBN-pm-GFP and CRY2-Rho1DN proteins, *CIBN-pm-GFP; CRY2-Rho1DN* females were crossed to males from the *Maternal-Tubulin-Gal4* line 67.15 to generate *CIBN-pm-GFP/67; CRY2-Rho1DN/15* females ("*67*" and "*15*" refer to *Maternal-Tubulin-Gal4* on chromosome II and III, respectively (Hunter and Wieschaus, 2000)). To generate embryos containing maternally deposited CIBN-pm (without GFP) and CRY2-Rho1DN proteins, *CIBN-pm; CRY2-Rho1DN* females were crossed to *67.15* males to generate *CIBN-pm/+; +/67; CRY2-Rho1DN/15* females. In both cases, embryos derived from the F1 females were used in the optogenetic experiments. The use of CIBN-pm without a GFP tag was to allow better visualization of GFP-tagged myosin regulatory light chain Sqh. The following *Maternal-Tubulin-Gal4* lines were used: (1) *67; 15*, (2) *67 Sqh-mCherry; 15 Sqh-GFP*, (3) *67 Sqh-mCherry; 15 E-cadherin-GFP*, (4) *67 Sqh-GFP; 15*, (5) *67 Sqh-GFP; 15 Sqh-GFP*, (6) *67 Sqh-mCherry; 15 Utrophin-Venus*, and (7) *67 Sqh-GFP; 15 P4M-mCherry*. Specifically:

- Figure 1c, d, and g, Figure 1 – figure supplement 1: *CIBN-pm-GFP; CRY2-Rho1DN* females were crossed to *67; 15* males.
- Figure 1f: *CIBN-pm; CRY2-Rho1DN* females were crossed to *67 Sqh-GFP; 15* males.
- Figure 2a: *CIBN-pm* females were crossed to *67 Sqh-mCherry; 15 Utrophin-Venus* males.
- Figure 2b: *CIBN-pm; CRY2-Rho1DN* females were crossed to *67 Sqh-mCherry; 15 Utrophin-Venus* males.
- Figure 3: *CIBN-pm; CRY2-Rho1DN* females were crossed to *67 Sqh-mCherry; 15 E-cadherin-GFP* males.
- Figure 4, Figure 5, Figure 4 – figure supplement 1-2, Figure 5 – figure supplement 1, Figure 6 – figure supplement 1, Figure 8 – figure supplement 1: *CIBN-pm-GFP; CRY2-Rho1DN* females were crossed to *67 Sqh-mCherry; 15 Sqh-GFP* males.
- Figure 4 – figure supplement 3a: *CIBN-pm; CRY2-Rho1DN* females were crossed to *67 Sqh-mCherry; 15 Sqh-GFP* males.
- Figure 4 – figure supplement 3c: *CIBN-pm; CRY2-Rho1DN* females were crossed to *67 Sqh-GFP; 15 Sqh-GFP* males.
- Figure 9f-g: *CIBN-pm; CRY2-Rho1DN* females were crossed to *67 Sqh-GFP; 15 P4M-mCherry* males.

Viability test for Opto-Rho1DN embryos

Embryo viability test was performed by hand selecting cellularizing embryos derived from *67/CIBNpm-GFP; 15/CRY2-Rho1DN* female flies in a dark room where the only illuminating light is red light. The selected embryos were randomly divided into two groups and placed on two fresh apple juice plates. One plate was kept in dark and the other was placed under a beam of

white light with moderate intensity. Plates were kept at 18 °C for more than 48 hours, after which the hatched and unhatched embryos were counted using a Nikon stereo microscope. Three independent trails were conducted. In total, 60 out of 70 stimulated embryos did not hatch whereas all 63 unstimulated embryos hatched.

Live imaging and optogenetic stimulation

To prepare embryos for live imaging, embryos were manually staged and collected from apple juice plates, and dechorionated with ~3% bleach in a dark room using an upright Nikon stereo microscope. In optogenetic experiments, embryos were protected from unwanted stimulation using an orange-red light filter placed on top of white light coming from the stereo microscope. After dechorionation, embryos were rinsed thoroughly with water, and transferred on a 35 mm glass-bottom dish (MatTek Corporation). Distilled water was then added to the dish well to completely cover the embryos. Live imaging was performed in water at room temperature with one of the following approaches.

To examine the plasma membrane recruitment of CRY2-Rho1DN and its impact on cortical association of myosin (Figure 1c-f), embryos were imaged using a Nikon inverted spinning disk confocal microscope equipped with the perfect focus system and Andor W1 dual camera, dual spinning disk module. An CFI Plan Apo Lambda 60×/1.40 WD 0.13 mm oil objective lens was used for imaging. For membrane recruitment of CRY2-Rho1DN, time lapse movies were taken for post-cellularization embryos at a single z-plane close to the apical side of the tissue at a frame rate of 0.46 s per frame. For cortical association of myosin, a small z-stack (5 slices, 0.5 μm step size) were taken at a rate of 3.46 s per stack. The image size is 858 by 1536 pixels with a lateral

pixel size of 0.11 μm, which corresponds to a 94-μm by 169-μm region. For each embryo, pre-stimulation images were acquired using a 561-nm laser, which did not activate Opto-Rho1DN. Stimulation and post-stimulation imaging were performed simultaneously as we subsequently imaged the embryo with both 488-nm and 561-nm lasers in an alternating pattern using triggered excitation.

To examine the spatial confinement of stimulation (Figure 1g) and the effect of activation of Opto-Rho1DN on apical constriction during ventral furrow formation (Figure 1 – figure supplement 1), embryos were imaged on a Leica SP5 confocal microscope with a 63×/1.3 NA glycerin-immersion objective lens. A 2× zoom was used. 20 confocal z-sections with a step size of 1 μm were acquired every 13 s. The image size is 1024×512 pixels with a lateral pixel size of 240 nm. The total imaged volume is approximately 246×123×19 μm. First, a single-time-point pre-stimulated image stack was acquired using a 561-nm laser. Next, stimulation was performed by taking a single-time-point image stack using both 488-nm and 561-nm lasers, which took 13 s. Stimulation was followed by post-stimulation acquisition with 561-nm laser for 20 time points (260 s). The stimulation and post-stimulation acquisition cycle was repeated until the end of the movie (i.e., stimulated for 13 s every 273 s).

To examine the rate of tissue recoil after laser ablation (Figure 3), embryos were imaged on an Olympus FVMPE-RS multiphoton system with a 25×/1.05 numerical aperture water immersion objective lens. For unstimulated embryos, a pre-ablation Z-stack was obtained using a 1040-nm laser to image a 512×100-pixel region (171×33 μm, 3× zoom) with a step size of 2 μm, which took approximately 16 s. Laser intensity increased linearly (4-7%) from the surface of the

embryo to 100-μm deep. This pre-ablation Z-stack was used to determine the stage of the embryo. Next, a 10-frame single Z-plane pre-ablation movie was obtained with 1040-nm laser. A 512×512-pixel region (171×171 μm, 3× zoom) was imaged, which took approximately 1s per frame. Next, a 920-nm laser with 30% laser intensity was used to ablate a 3D region from immediately below the vitelline membrane to ~ 20 μm deep. This was achieved by taking a Z-stack with a step size of 1.5 μm. The ROI of the ablated region is ~3 μm along the A-P axis. The purpose of targeting multiple Z-planes for ablation was to ensure that the very apical surface of the ventral cells was ablated. This was particularly important for the stimulated embryos since the ventral cells undergo rapid apical relaxation after Rho1 inhibition. Immediately after laser ablation, a 100-frame single Z-plane post-ablation movie was acquired using both 1040-nm and 920-nm lasers. The same ROI was imaged as the pre-ablation single Z-plane movie with identical image acquisition speed. For stimulated embryos, a stimulation procedure was included before laser ablation. First, a Z-stack was acquired to determine the stage of the embryo, as described above. Then, a 458-nm diode laser with 0.3% laser intensity was used to illuminate the whole embryo under 1× digital zoom for 12 s to activate the optogenetic module. A three-minute wait time was applied after stimulation to ensure the complete inactivation of myosin and disassembly of apical F-actin before laser ablation. Following this wait time, the same laser ablation procedure as used for the unstimulated embryos was applied (pre-ablation single Z-movie, laser ablation, and post-ablation single Z-movie), except that both 1040-nm and 920-nm lasers were used for acquiring the pre-ablation movie.

The analyses of F-actin (Utrophin-Venus) after Opto-Rho1DN activation (Figure 2) and the stage-specific effect of Opto-Rho1DN activation on ventral furrow invagination (Figure 4) were

conducted using the following imaging protocol. Embryos were imaged on the Olympus FVMPE-RS multiphoton system with a 25×/1.05 numerical aperture water immersion objective lens. Pre-stimulation images were obtained by using a 1040-nm laser to excite a 512×100-pixel region (171×33 μm, 3× zoom). Continuous imaging was conducted for pre-stimulation imaging. For each time point, a 100-μm Z-stack with step size of 1μm was obtained with linearly increased laser intensity (4%-7.5%) over Z, which took 34 s. Stimulation was performed at different stages of ventral furrow formation using a 458-nm single-photon diode laser by illuminating the whole embryo under 1× zoom for 12 s with 0.3% laser intensity. A wait period of ~ 20 s was imposed after stimulation for examine the stage-specific effect. Post-stimulation images were obtained using both 1040-nm and 920-nm lasers. Same setting as pre-stimulation imaging was applied, with an addition of a linear increase in 920-nm laser intensity (0.1%-0.5%) over Z. Stimulation was conducted manually every 5 stacks during post-stimulation imaging (i.e., stimulation for 12 s every ~200 s) to ensure the sustained membrane recruitment of CRY2-Rho1DN.

To image wildtype and *snail* mutant embryos for the volume measurement in the lateral ectoderm (Vol_{ec}, Figure 8), embryos were imaged on the Olympus FVMPE-RS multiphoton system with a 25×/1.05 numerical aperture water immersion objective lens. Z stacks of 120 μm with a step size of 1 μm was acquired continuously over a 512×150-pixel region (256×75 μm, 2× zoom). A 920-nm laser with a linear increase of laser intensity over Z (0.3-2.5%) was used for imaging. The temporal resolution of the movie was ~54 s/stack. *halo snail* homozygous mutant embryos were derived from the *halo snail*/*CyO, Sqh-GFP* stock and were recognized based on the "halo" phenotype during cellularization.

To examine ectodermal cell movement after Opto-Rho1DN activation (Figure 9f-g), embryos were imaged on the Olympus FVMPE-RS multiphoton system with a 25×/1.05 numerical aperture water immersion objective lens. A pre-stimulation Z stack was acquired using 1040-nm laser to illuminate a ROI (512×150 pixel, 171×50 μm, 3× zoom) with a step size of 1 μm for a total depth of 100 μm. The laser intensity increased linearly over Z (3-7%). Next, whole embryo stimulation was achieved by illuminating the embryo with a 458-nm laser at 0.3% laser intensity for ~12 s under 1× zoom. Post-stimulation Z stacks were acquired using similar protocol as the pre-stimulation Z stack, except that both 920-nm and 1040-nm lasers were used for imaging. The intensity of the 920-nm laser also increased linearly over Z (0.5%-2.5%). The temporal resolution of the post-stimulation movie was ~ 41 s/stack. At the end of each experiment, a single frame image of the embryo was acquired at 1× zoom to record the A-P orientation of the embryo.

Image analysis and quantification

All image processing and analysis were processed using MATLAB (The MathWorks) and ImageJ (NIH).

To quantify the percent membrane recruitment of CRY2-Rho1DN after stimulation (Figure 1d), cell membrane was segmented based on the CIBN-pm-GFP signal using a custom MATLAB code. The resulting membrane mask was used to determine the signal intensity of CRY2-Rho1DN (mCherry tagged) along the cell membrane over time. The intensity of the CRY2-Rho1DN signal in the cytoplasm, which is determined as the average intensity in the cells before

stimulation, was subtracted from the measured intensity. The resulting net membrane signal intensity was further normalized by scaling between 0 and 1.

To quantify the rate of tissue recoil after laser ablation (Figure 3), the width change of the ablated region along the A-P axis was measured over time from the kymograph using ImageJ. The width change during the first 20 s after laser ablation (when the change over time was relatively linear) was reported to indicate the rate of tissue recoil.

The invagination depth D (i.e., the distance between the vitelline membrane and the apex of the ventral-most cell, e.g., Figure 4b) and the apical-basal length of the ventral cells over the course of ventral furrow formation (Figure 4 – figure supplement 1a, b) were manually measured from the cross-section view of the embryos using ImageJ.

To categorize embryo responses to stage-specific Opto-Rho1DN stimulation, first, each post-stimulation movie was aligned to a representative control movie based on the intermediate furrow morphology at the time of stimulation. The purpose of this alignment was to minimize the impact of embryo-to-embryo variation in $T_{L\text{-}S\ trans}$ (Figure 4 – figure supplement 1d). The resulting aligned time was used in the analysis because it provided a better measure of the stage of ventral furrow formation than the "absolute" time defined by the onset of gastrulation in each embryo. Next, dD/dt immediately after stimulation are determined by a linear fitting of D over time in the first 4 minutes after stimulation (Figure 4 – figure supplement 1f). Embryos with $dD/dt < -0.3$ μm/min are defined as Early Group. These embryos undergo tissue relaxation and result in decrease in D over time. Embryos with dD/dt between -0.3 μm/min and 0.3 μm/min are

defined as Mid Group. These embryos do not undergo obvious tissue relaxation but display a temporary pause before they continue to invaginate. Embryos with $dD/dt > 0.3$ µm/min are defined as Late Group. These embryos continue to invaginate despite the rapid inactivation of myosin. To quantify the impact of myosin inhibition on furrow invagination (Figure 4d), the delay time in furrow invagination (T_{delay}) was measured. T_{delay} is defined as the difference in time for a given stimulated embryo to reach a D of 20µm compared to a representative control embryo.

To examine the change of apical cell area of the flanking, non-constricting cells in stimulated Opto-Rho1DN embryos (Figure 4 – figure supplement 2a, b), a custom MATLAB script was used to generate a flattened surface view of the embryo which accounts for the curvature of the embryo. The apical cell area was measured by manually tracking and outlining flanking cells followed by area measurement using ImageJ.

To segment the mesoderm cells (Figure 5), Carving procedure from ilastik (Berg et al., 2019) was used in combination with manual correction using ImageJ and MATLAB to segment and reconstitute the 3D shape of individual cells. Cell length was calculated by summing up the distance between neighboring centroids at consecutive z planes to account for the curvature of the cell. Apical surface area was calculated based on the intersection area between the curved apical surface of the tissue and the 3D object of the cell. This intersection area was determined using a custom MATLAB code. The lateral surface area was calculated by a subtraction of the apical and basal surface area from the overall cell surface area, which was calculated from the 3D object of the cell. The volume is calculated directly from the 3D object of the cell.

To evaluate the volume flux in the lateral ectoderm region (Figure 8), pixel segmentation procedure from ilastik (Berg et al., 2019) was used to segment a fixed lateral ectoderm region (ROI: from 60° to 120° away from the ventral midline and 75 μm long along the AP axis) in both WT and *snail* mutant embryos. Segmentation was performed based on Sqh-GFP signal which clearly defines the apical and basal boundaries of the tissue. The tissue was segmented as a continuum without segmentation of individual cells. The volume of the selected ROI ("Vol_{ex}") at each time point was determined based on the segmented 3D tissue object. To measure the movement of lateral ectoderm during gastrulation, the position of a cell initially located 50° away from the ventral midline at the onset of gastrulation was manually tracked over time using ImageJ.

To measure ectodermal shortening from 2D cross-section view of the embryos (Figure 8 – figure supplement 1), the thickness of the lateral ectoderm is reported as the cross-section area of the ectodermal cell layer between 60° and 90° from the dorsal-ventral axis, which provides a good readout of tissue volume redistribution in 3D. A custom MATLAB script was used to facilitate the measurement. Specifically, the apical surface of the tissue was determined by automatic segmentation of the vitelline membrane of the embryo. The resulting curve was subsequently fit into a circle ("the outer membrane circle"). The basal surface of the tissue was determined by automatic segmentation and tracking of the basal myosin signal, with necessary manual corrections when the basal signal became too dim to be segmented accurately. Tissue thickness was measured as the cross-section area of a section of the ectodermal tissue bounded by the outer

membrane, the basal surface, and two radii of the outer membrane circle that are 60° and 90° away from the ventral midline, respectively.

To detect ectodermal cell movement in Early Group embryos after stimulation (Figure 9a-e), kymographs were generated from the surface views with the CIBN-pmGFP signal that marks the cell membrane. Individual membrane traces within the first six minutes after stimulation were manually tracked from the kymograph using the line selection tool in ImageJ. The slope of the lines was subsequently measured using ImageJ to calculate the rate of membrane movement, which was then plotted against the position of corresponding membrane relative to the ventral midline at the time of stimulation. The average velocity of tissue movement at ventral mesodermal (from -10 to -40 μm and from 10 to 40 μm) or lateral ectodermal (from -60 to -120 μm and from 60 to 120 μm) regions of the embryos was calculated and tested using one-tailed one-sample t-test against 0.

Energy minimization-based vertex model for ventral furrow formation (Polyakov et al model)

The 2D vertex model for ventral furrow formation, which considers the cross-section view of the embryo, was constructed as previously described (Polyakov et al., 2014). In brief, the model contains a ring of 80 cells that represent the cross-section of an actual embryo. The initial geometry of the cells in the model resembles that in the real embryo. The apical, basal and lateral membranes of the cells are modeled as elastic springs that resist deformation, and the cells have a propensity to remain constant cell volume (area in 2D). In the model, apical constriction provides the sole driving force for tissue deformation, which is achieved by allowing the apex of

the cells in the ventral region of the embryo to shrink. The resulting morphological changes of the tissue are determined by the stiffness of the apical, lateral, and basal springs, cell volume conservation, and a stepwise reduction of basal spring stiffness (see below).

The energy equation that approximates the mechanical properties of the system is described by the following expression:

$$E = \sum_i \varphi_i \mu_i a_i^2 + \sum_i [K_l(l_i - l_0)^2 + K_b(b_i - b_0)^2 + K_a(a_i - a_0)^2]$$
$$+ \sum_i C_{VOL}(V_i) + C_{YOLK}(V_{yolk})$$

The first term in the equation stands for myosin mediated apical constriction. The term $\varphi_i \mu_i$ defines the spatial distribution of myosin contractility. φ_i equals to 1 for cells within the mesoderm domain (9 cells on each side of the ventral midline, a total of 18 cells) and 0 for the rest of cells, which ensures that only the mesodermal cells will constrict apically. μ_i is a Gaussian function that peaks at the ventral midline. Specifically,

$$\mu_i = \mu_0 e^{\frac{-(i-i_{mid})^2}{2\sigma^2}}$$

Here i_{mid} stands for the cell ID at the ventral midline, μ_0 defines the strength of apical constriction and σ defines the width of the force distribution. Note that due to the Gaussian-shaped force distribution, only 12 cells at the ventral most region of the embryo will undergo apical constriction, similar to what occurs in the real embryo.

The second term in the equation stands for the elastic resistance of the membranes. a_i, b_i, and l_i stand for the area (length in 2D) of the apical, basal and lateral membrane of cell i, respectively.

a_0, b_0, and l_0 are the corresponding resting length, which are set to be their initial length. k_a, k_b and k_l are the spring constant of the apical, basal and lateral springs, respectively.

The third and fourth terms, C_{VOL} and C_{YOLK}, are constraint functions that describe volume conservation of the cells and the yolk, respectively. These two terms impose penalties when the volume deviates from the resting value. Specifically,

$$C_{VOL}(V_i) = K_v(V_i - V_0)^2$$

$$C_{YOLK}(V_{yolk}) = K_Y(V_{yolk} - V_{0,yolk})^2$$

Here, V_i stands for the volume of cell i. V_0 stands for the initial equilibrium volume of cell i. Similarly, V_{yolk} stands for the volume of the yolk. $V_{0,yolk}$ stands for the initial equilibrium volume of the yolk. K_v and K_{yolk} control the deviation of the cell volume and the yolk volume from the initial equilibrium values, respectively.

In the simulation, the basal rigidity of the epithelium (K_b) decreases adiabatically, allowing the model to transition through a series of intermediate equilibrium states defined by the specific K_b values. These intermediate states recapitulate the lengthening-shortening dynamics of the constricting cells observed in the real embryos (Polyakov et al., 2014).

To produce an in-plane compressive stress in the ectodermal tissue, we set the resting length of the lateral springs (l_0) 20% shorter than their original length. Because of the cell volume conservation constraint, shortening of the ectodermal cells in the apical-basal direction will result in an expansion of cells in the orthogonal direction, which is the planar direction of the epithelium. This expansion provides a mechanism to produce in-plane compressive stress in the

epithelial sheet. As shown in Figure 8 – figure supplement 2, when the percent reduction of the ectodermal cell length is lowered from 20% to 10%, the binary response to acute actomyosin inhibition is still present, although the final depth of the furrow in the simulated Late Group embryo is reduced. Further lowering the percent reduction to 5% abolishes the binary response.

To simulate the optogenetic inhibition of myosin contractility in the model, we set the program such that the apical contractility term will be reduced to zero at defined intermediate equilibrium state. This approach allows us to inhibit apical contractility at any intermediate furrow configuration specified by K_b.

In order to simulate the impact of impairing apical constriction on invagination, we modified our model in two different ways. First, to reduce the number of apically constricting cells, we decreased the width of the Gaussian function that defines the spatial distribution of apical myosin contractility. Second, to recapitulate the weakened and uncoordinated apical constriction observed in certain apical constriction mutants, we inhibited apical constriction from every other cell within the ventral 18-cell region.

In order to account for the impact of optogenetic stimulation of Opto-Rho1DN on lateral myosin in the constricting cells, we implemented an active lateral constriction force along the lateral edges of the constricting cells, on top of the passive lateral restoration force described above. In such a scenario, the active and passive lateral forces worked in combination to mediate ventral cell shortening, but only the active force was sensitive to myosin inactivation. For each lateral cortex within the constriction domain, the active lateral constriction force is generated by a

spring with a resting length of zero. The lateral shortening force in the constricting cells is determined by:

$$F_{shortening} = K_{L_active} l + K_{L_passive}(l - l_0)$$

Where K_{L_active} and $K_{L_passive}$ are the spring constant of the active and passive lateral springs, respectively, and l and l_0 are the current and the resting length of the lateral edges, respectively. As shown in Figure 7, A spring constant of $K_{L_active} = 2$ generated the desired furrow morphology under a broad range of passive spring constant ($K_{L_passive}$= [0.002, 20]). A further increase of K_{L_active} result in deeper furrows as more cells are incorporated into the neck region of the furrow. To account for the observation that lateral myosin in the constricting cells rapidly diminishes after Opto-Rho1DN activation, K_{L_active} is set to zero after in silico myosin inhibition.

List of parameters used in Figure 6c:

Parameter	***Value***
K_a	30
K_l	20
K_b *	$2^{10} \rightarrow 2^0$
μ_0 **	5000
σ	3
K_v	5000
K_Y	1

*: In the simulation, K_b decreases adiabatically from 2^{10} to 2^0, with a 2-fold reduction at each step. An energy equilibrium state is reached for each value of K_b. These energy equilibrium states define the intermediate and final furrow morphology.

**: The model recapitulates the binary response to acute loss of actomyosin contractility under a wide range of μ_0 tested (500 – 50,000).

Statistics

Sample sizes for the presented data and methods for statistical comparisons can be found in figure legends. *p* values were calculated using MATLAB ttest2 or ranksum function.

Acknowledgements:

We thank members of the He lab and the Griffin lab at Dartmouth College for sharing valuable thoughts during this work; James Moseley and Magdalena Bezanilla for providing constructive suggestions and comments on the manuscript; Ann Lavanway for imaging support. We thank the Wieschaus lab and the De Renzis lab for sharing reagents, Oleg Polyakov for sharing the code for the energy minimization-based vertex model, and the Bloomington Drosophila Stock Center for fly stocks. This study is supported by NIGMS ESI-MIRA R35GM128745 and American Cancer Society Institutional Research Grant #IRG –82-003-33 to B.H.. The study used core services supported by STANTO15R0 (CFF RDP), P30-DK117469 (NIDDK P30/DartCF), and P20-GM113132 (bioMT COBRE).

Declaration of Interests:

The authors declare no competing interests.

References

Allena R, Mouronval AS, Aubry D. Simulation of multiple morphogenetic movements in the Drosophila embryo by a single 3D finite element model. J Mech Behav Biomed Mater 2010;3:313–23.

Barrett K, Leptin M, Settleman J. The Rho GTPase and a putative RhoGEF mediate a signaling pathway for the cell shape changes in Drosophila gastrulation. Cell 1997;91:905–15.

Berg, S., Kutra, D., Kroeger, T., Straehle, C. N., Kausler, B. X., Haubold, C., Schiegg, M., Ales, J., Beier, T., Rudy, M., et al. (2019). ilastik: interactive machine learning for (bio)image analysis. Nat Methods 16, 1226–1232.

Brodland GW, Conte V, Cranston PG, Veldhuis J, Narasimhan S, Hutson MS, et al. Video force microscopy reveals the mechanics of ventral furrow invagination in Drosophila. Proc Natl Acad Sci U A 2010;107:22111–6.

Chanet S, Martin AC. Mechanical force sensing in tissues. Prog Mol Biol Transl Sci 2014;126:317–52.

Chen W, He B. A feedback mechanism mediated by myosin II-dependent apical targeting of Rab11 vesicles reinforces apical constriction. bioRxiv 2021. https://doi.org/10.1101/2021.03.07.434309

Conte V, Munoz JJ, Baum B, Miodownik M. Robust mechanisms of ventral furrow invagination require the combination of cellular shape changes. Phys Biol 2009;6:016010.

Conte V, Ulrich F, Baum B, Munoz J, Veldhuis J, Brodland W, et al. A biomechanical analysis of ventral furrow formation in the Drosophila melanogaster embryo. PLoS One 2012;7:e34473.

Coravos JS, Martin AC. Apical Sarcomere-like Actomyosin Contracts Nonmuscle Drosophila Epithelial Cells. Dev Cell 2016;39:346–58. https://doi.org/10.1016/j.devcel.2016.09.023.

Costa M, Wilson ET, Wieschaus E. A putative cell signal encoded by the folded gastrulation gene coordinates cell shape changes during Drosophila gastrulation. Cell 1994;76:1075–89.

Dawes-Hoang RE, Parmar KM, Christiansen AE, Phelps CB, Brand AH, Wieschaus EF. folded gastrulation, cell shape change and the control of myosin localization. Development 2005;132:4165–78.

Doubrovinski K, Swan M, Polyakov O, Wieschaus EF. Measurement of cortical elasticity in Drosophila melanogaster embryos using ferrofluids. Proc Natl Acad Sci U S A. 2017; 114(5):1051-1056.

Edgar BA, Lehman DA, O'Farrell PH. Transcriptional regulation of string (cdc25): a link between developmental programming and the cell cycle. Dev Camb Engl 1994;120:3131–43.

Etienne-Manneville S, Hall A. Rho GTPases in cell biology. Nature 2002;420:629–35. https://doi.org/10.1038/nature01148.

Feig LA, Cooper GM. Inhibition of NIH 3T3 cell proliferation by a mutant ras protein with preferential affinity for GDP. Mol Cell Biol 1988;8:3235–43. https://doi.org/10.1128/mcb.8.8.3235.

Figard L, Sokac AM. Imaging cell shape change in living Drosophila embryos. J Vis Exp 2011;(49):2503.

Foe VE, Alberts BM. Studies of nuclear and cytoplasmic behaviour during the five mitotic cycles that precede gastrulation in Drosophila embryogenesis. J Cell Sci 1983;61:31–70.

Gelbart MA, He B, Martin AC, Thiberge SY, Wieschaus EF, Kaschube M. Volume conservation principle involved in cell lengthening and nucleus movement during tissue morphogenesis. Proc Natl Acad Sci U A 2012;109:19298–303.

Gheisari E, Aakhte M, Müller H-AJ. Gastrulation in Drosophila melanogaster: Genetic control, cellular basis and biomechanics. Mech Dev 2020;163:103629. https://doi.org/10.1016/j.mod.2020.103629.

Gilmour D, Rembold M, Leptin M. From morphogen to morphogenesis and back. Nature 2017;541:311–20. https://doi.org/10.1038/nature21348.

Gracia M, Theis S, Proag A, Gay G, Benassayag C, Suzanne M. Mechanical impact of epithelial-mesenchymal transition on epithelial morphogenesis in Drosophila. Nat Commun 2019;10:2951. https://doi.org/10.1038/s41467-019-10720-0.

Groth AC, Fish M, Nusse R, Calos MP. Construction of transgenic Drosophila by using the site-specific integrase from phage phiC31. Genetics 2004;166:1775–82.

Guglielmi G, Barry JD, Huber W, De Renzis S. An Optogenetic Method to Modulate Cell Contractility during Tissue Morphogenesis. Dev Cell 2015;35:646–60.

Hacker U, Perrimon N. DRhoGEF2 encodes a member of the Dbl family of oncogenes and controls cell shape changes during gastrulation in Drosophila. Genes Dev 1998;12:274–84.

He B, Doubrovinski K, Polyakov O, Wieschaus E. Apical constriction drives tissue-scale hydrodynamic flow to mediate cell elongation. Nature 2014;508:392–6.

Heisenberg C-P, Bellaïche Y. Forces in tissue morphogenesis and patterning. Cell 2013;153:948–62. https://doi.org/10.1016/j.cell.2013.05.008.

Homem CCF, Peifer M. Diaphanous regulates myosin and adherens junctions to control cell contractility and protrusive behavior during morphogenesis. Development 2008;135:1005–18. https://doi.org/10.1242/dev.016337.

Hunter C, Wieschaus E. Regulated expression of nullo is required for the formation of distinct apical and basal adherens junctions in the Drosophila blastoderm. J Cell Biol 2000;150:391–401.

Jin Qiu, Lang JH, Slocum AH. A curved-beam bistable mechanism. J Microelectromechanical Syst 2004;13:137–46. https://doi.org/10.1109/JMEMS.2004.825308.

John, A. and Rauzi, M. (2021). A two-tier junctional mechanism drives simultaneous tissue folding and extension. Dev Cell 56, 1469-1483.e5.

Johndrow JE, Magie CR, Parkhurst SM. Rho GTPase function in flies: insights from a developmental and organismal perspective. Biochem Cell Biol Biochim Biol Cell 2004;82:643–57. https://doi.org/10.1139/o04-118.

Kennedy MJ, Hughes RM, Peteya LA, Schwartz JW, Ehlers MD, Tucker CL. Rapid blue-light-mediated induction of protein interactions in living cells. Nat Methods 2010;7:973–5. https://doi.org/10.1038/nmeth.1524.

Kerridge S, Munjal A, Philippe JM, Jha A, de las Bayonas AG, Saurin AJ, et al. Modular activation of Rho1 by GPCR signalling imparts polarized myosin II activation during morphogenesis. Nat Cell Biol 2016;18:261–70.

Kolsch V, Seher T, Fernandez-Ballester GJ, Serrano L, Leptin M. Control of Drosophila gastrulation by apical localization of adherens junctions and RhoGEF2. Science 2007;315:384–6.

Leptin M. twist and snail as positive and negative regulators during Drosophila mesoderm development. Genes Dev 1991;5:1568–76.

Leptin M, Grunewald B. Cell shape changes during gastrulation in Drosophila. Development 1990;110:73–84.

Liu H, Yu X, Li K, Klejnot J, Yang H, Lisiero D, et al. Photoexcited CRY2 interacts with CIB1 to regulate transcription and floral initiation in Arabidopsis. Science 2008;322:1535–9. https://doi.org/10.1126/science.1163927.

Magie CR, Meyer MR, Gorsuch MS, Parkhurst SM. Mutations in the Rho1 small GTPase disrupt morphogenesis and segmentation during early Drosophila development. Dev Camb Engl 1999;126:5353–64.

Manning AJ, Peters KA, Peifer M, Rogers SL. Regulation of epithelial morphogenesis by the G protein-coupled receptor mist and its ligand fog. Sci Signal 2013;6:ra98.

Mao Y, Baum B. Tug of war--the influence of opposing physical forces on epithelial cell morphology. Dev Biol 2015;401:92–102. https://doi.org/10.1016/j.ydbio.2014.12.030.

Martin AC. The Physical Mechanisms of Drosophila Gastrulation: Mesoderm and Endoderm Invagination. Genetics 2020;214:543–60. https://doi.org/10.1534/genetics.119.301292.

Martin AC, Gelbart M, Fernandez-Gonzalez R, Kaschube M, Wieschaus EF. Integration of contractile forces during tissue invagination. J Cell Biol 2010;188:735–49.

Martin AC, Goldstein B. Apical constriction: themes and variations on a cellular mechanism driving morphogenesis. Development 2014;141:1987–98.

Martin AC, Kaschube M, Wieschaus EF. Pulsed contractions of an actin-myosin network drive apical constriction. Nature 2009;457:495–9.

Mason FM, Tworoger M, Martin AC. Apical domain polarization localizes actin-myosin activity to drive ratchet-like apical constriction. Nat Cell Biol 2013;15:926–36.

Munjal A, Lecuit T. Actomyosin networks and tissue morphogenesis. Development 2014;141:1789–93.

Munjal A, Philippe JM, Munro E, Lecuit T. A self-organized biomechanical network drives shape changes during tissue morphogenesis. Nature 2015;524:351–5.

Munoz JJ, Barrett K, Miodownik M. A deformation gradient decomposition method for the analysis of the mechanics of morphogenesis. J Biomech 2007;40:1372–80.

Nelson CM. On Buckling Morphogenesis. J Biomech Eng 2016;138:021005. https://doi.org/10.1115/1.4032128.

Nikolaidou KK, Barrett K. A Rho GTPase signaling pathway is used reiteratively in epithelial folding and potentially selects the outcome of Rho activation. Curr Biol 2004;14:1822–6.

Oda H, Tsukita S. Real-time imaging of cell-cell adherens junctions reveals that Drosophila mesoderm invagination begins with two phases of apical constriction of cells. J Cell Sci 2001;114:493–501.

Parks S, Wieschaus E. The Drosophila gastrulation gene concertina encodes a G alpha-like protein. Cell 1991;64:447–58.

Perez-Mockus, G., Mazouni, K., Roca, V., Corradi, G., Conte, V. and Schweisguth, F. (2017). Spatial regulation of contractility by Neuralized and Bearded during furrow invagination in Drosophila. Nat Commun 8, 1594.

Polyakov O, He B, Swan M, Shaevitz JW, Kaschube M, Wieschaus E. Passive mechanical forces control cell-shape change during Drosophila ventral furrow formation. Biophys J 2014;107:998–1010.

Rauzi M, Krzic U, Saunders TE, Krajnc M, Ziherl P, Hufnagel L, et al. Embryo-scale tissue mechanics during Drosophila gastrulation movements. Nat Commun 2015;6:8677.

Rich A, Fehon RG, Glotzer M. Rho1 activation recapitulates early gastrulation events in the ventral, but not dorsal, epithelium of Drosophila embryos. ELife 2020;9. https://doi.org/10.7554/eLife.56893.

Roberts PJ, Mitin N, Keller PJ, Chenette EJ, Madigan JP, Currin RO, et al. Rho Family GTPase Modification and Dependence on CAAX Motif-signaled Posttranslational Modification*. J Biol Chem 2008;283:25150–63. https://doi.org/10.1074/jbc.M800882200.

Royou A, Sullivan W, Karess R. Cortical recruitment of nonmuscle myosin II in early syncytial Drosophila embryos: its role in nuclear axial expansion and its regulation by Cdc2 activity. J Cell Biol 2002;158:127–37.

Sawyer JM, Harrell JR, Shemer G, Sullivan-Brown J, Roh-Johnson M, Goldstein B. Apical constriction: a cell shape change that can drive morphogenesis. Dev Biol 2010;341:5–19.

Sebti SM, Der CJ. Searching for the elusive targets of farnesyltransferase inhibitors. Nat Rev Cancer 2003;3:945–51. https://doi.org/10.1038/nrc1234.

Sweeton D, Parks S, Costa M, Wieschaus E. Gastrulation in Drosophila: the formation of the ventral furrow and posterior midgut invaginations. Development 1991;112:775–89.

Wolpert L, Tickle C, Arias AM. Principles of Development. Oxford University Press; 2015.

Yevick HG, Miller PW, Dunkel J, Martin AC. Structural Redundancy in Supracellular Actomyosin Networks Enables Robust Tissue Folding. Dev Cell 2019;50:586-598.e3. https://doi.org/10.1016/j.devcel.2019.06.015.

Figures and Figure Legends

Figure 1

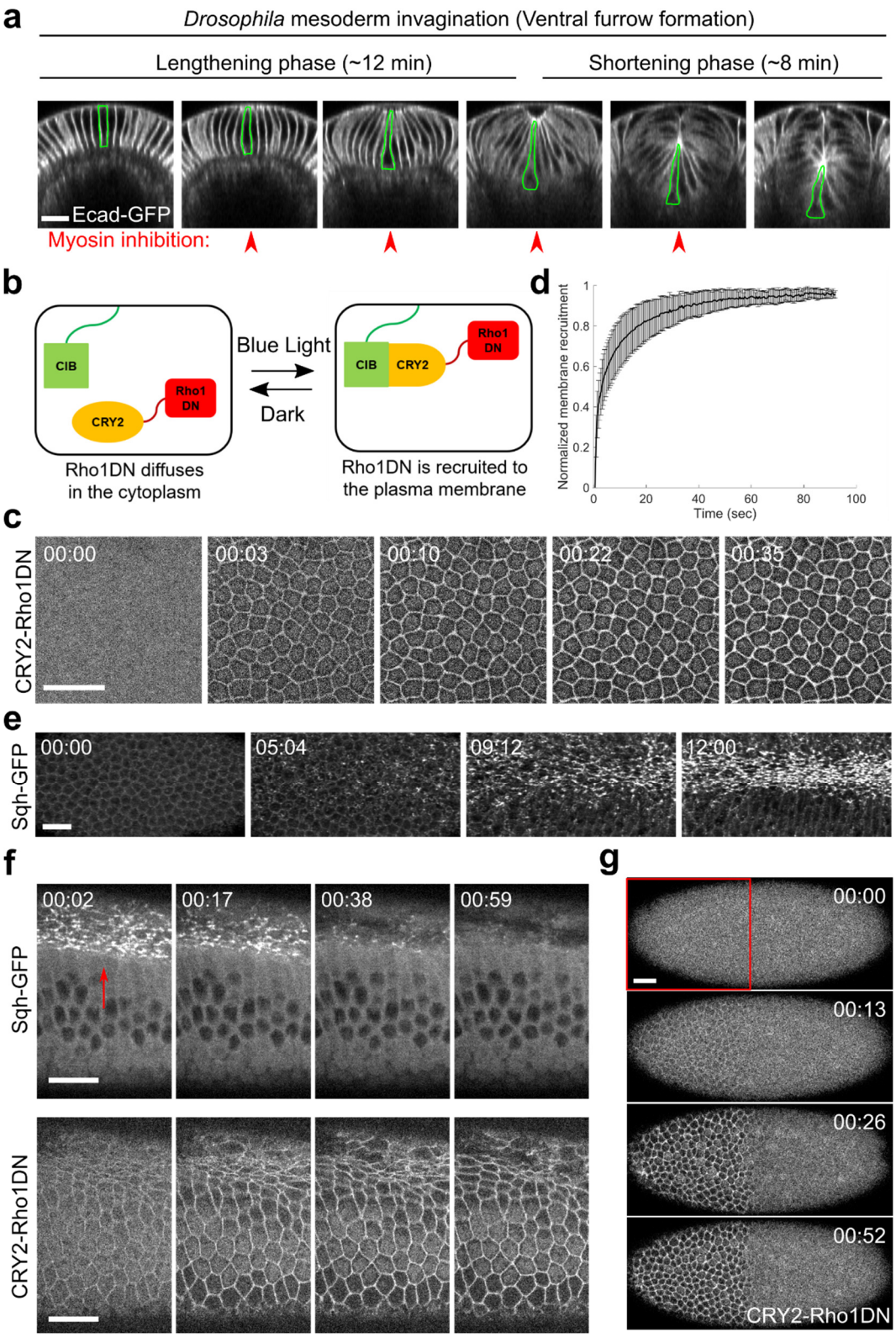

Figure 1. Light-dependent membrane recruitment of CRY2-Rho1DN results in rapid myosin inactivation. (a) *Drosophila* mesoderm invagination occurs in distinct lengthening and shortening phases. Ventral side is up (same for all cross-section images in this work unless otherwise stated). A single ventral cell undergoing apical constriction is outlined in green. In this study, we sought to test whether myosin contractility is required throughout the folding process by acute, stage-specific inhibition of Rho1 (arrowheads). **(b)** Cartoon depicting the principle of the optogenetic tool used in this study. Upon blue light stimulation, CRY2-Rho1DN is translocated from the cytosol to the plasma membrane through the interaction between CRY2 and membrane anchored CIBN. **(c)** Confocal images showing the rapid membrane recruitment of CRY2-Rho1DN upon blue light illumination. **(d)** Relative abundance of membrane recruited CRY2-Rho1DN over time after blue light stimulation. Error bar: s.d., N = 6 embryos. **(e)** A wildtype embryo expressing Sqh-GFP showing apical myosin accumulation during ventral furrow formation. N = 4 embryos. **(f)** Activation of Opto-Rho1DN results in rapid dissociation of myosin from the ventral cell cortex (arrow) in a gastrulating embryo. N = 8 embryos. **(g)** Confocal images showing the confined membrane recruitment of CRY2-Rho1DN within a region of interest (ROI, red box) that has been scanned by a focused beam of blue laser. N = 6 embryos. All scale bars = 20 μm.

Figure 1 - figure supplement 1

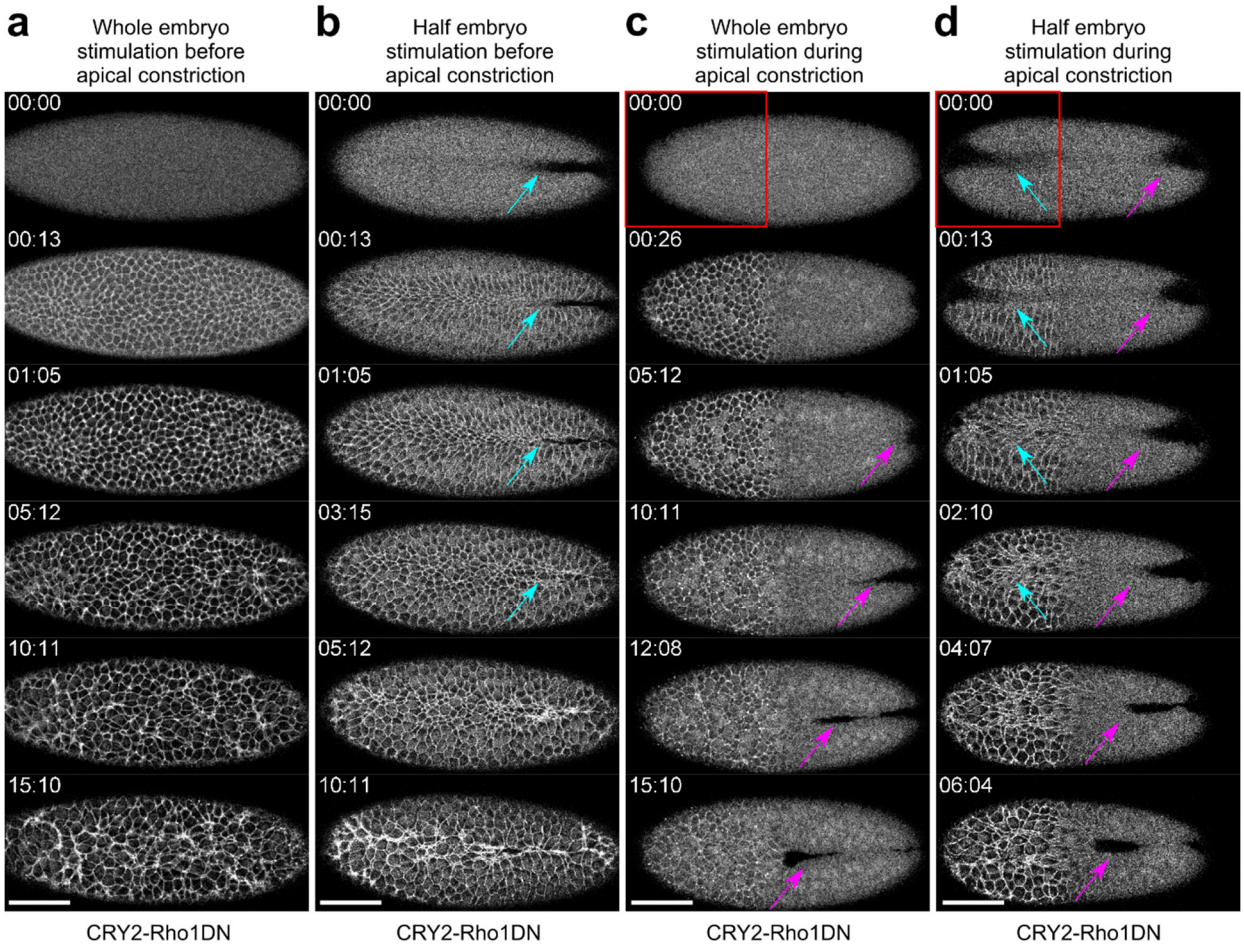

Figure 1 – figure supplement 1. Activation of Opto-Rho1DN inhibits apical constriction during gastrulation. Confocal images showing the effect of activating Opto-Rho1DN on apical constriction during ventral furrow formation. Time zero corresponds to the time of stimulation. N ≥ 2 embryos were tested for each condition. **(a)** Activating Opto-Rho1DN before the onset of gastrulation blocks apical constriction and ventral furrow formation. In the stimulated embryo, only a small set of cells scattered across the ventral domain undergo limited apical constriction over the course of 15 minutes. This is in contrast to the wildtype embryo where mesoderm invagination completes in 15 – 20 minutes. **(b)** Activating Opto-Rho1DN during apical constriction results in immediate relaxation of the constricted cells (cyan arrows). **(c)** Spatially confined activation of Opto-Rho1DN (red box) before gastrulation blocks apical constriction specifically in the stimulated region. Ventral furrow still forms in the unstimulated region of the embryo (magenta arrows). **(d)** Spatially confined activation of Opto-Rho1DN (red box) during apical constriction results in an immediate relaxation of the constricted cells specifically in the stimulated region (cyan arrows). Ventral furrow continues to form in the unstimulated region (magenta arrows). Scale bars: 50 µm.

Figure 2

a

Unstimulated

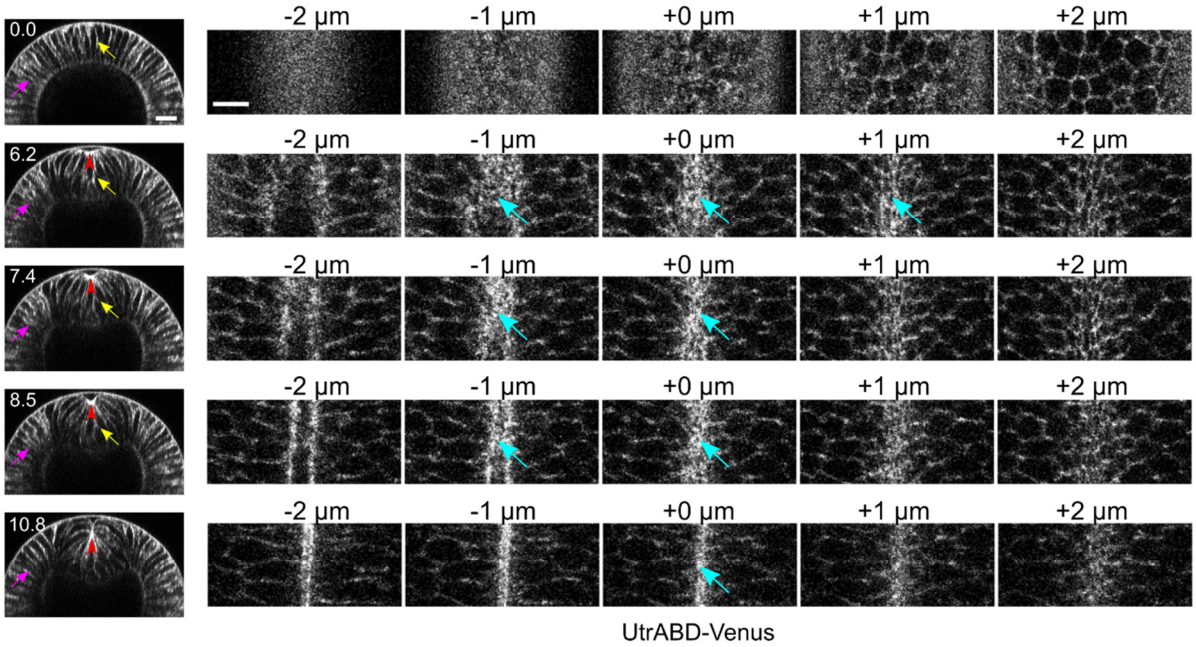

b Stimulated

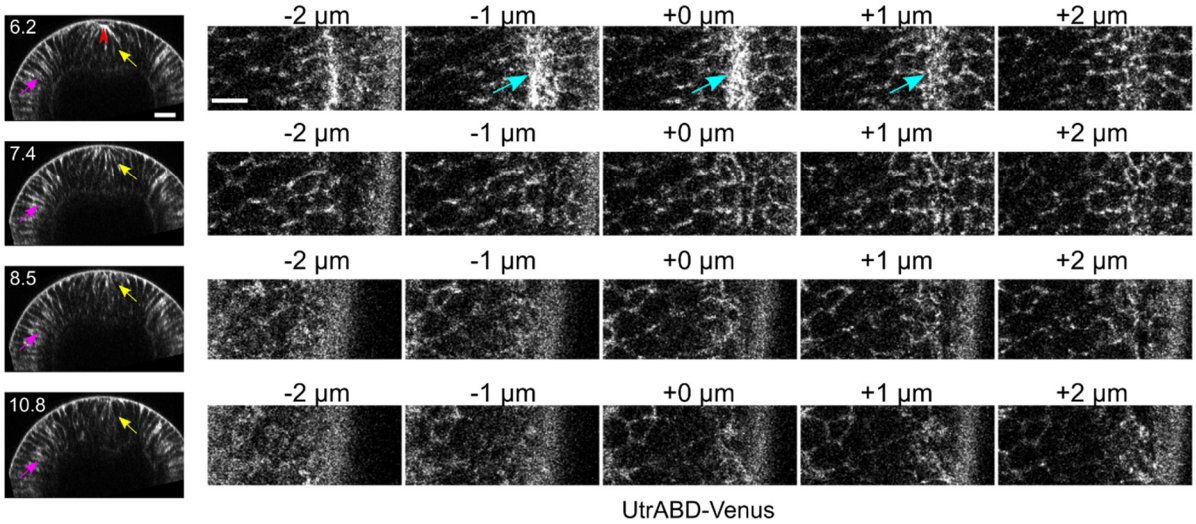

Figure 2. Rapid disassembly of apical F-actin in the constricting cells after Opto-Rho1DN stimulation. (a) Cross-sections (left) and en face views (right) of a representative unstimulated embryo showing the localization of the F-actin marker UtrophinABD-Venus (UtrABD-Venus) during ventral furrow formation. At the onset of apical constriction, F-actin is enriched along the lateral membrane in both mesodermal and ectodermal cells (yellow and magenta arrows, respectively). During apical constriction, F-actin also accumulates at the apical domain of the constricting cells (cyan arrows). T = 0 (min) is the onset of ventral furrow formation. +0 μm indicates the apex of the ventral most cells (red arrowheads) where the strongest accumulation of apical F-actin is observed. **(b)** Upon Opto-Rho1DN stimulation (immediately before 6.2 min), apical F-actin disappears within 1.2 minutes (cyan arrows). Lateral F-actin in the constricting cells was not immediately affected and only started to diminish 4 minutes after stimulation (yellow arrows). Lateral F-actin in the ectodermal cells was not significantly affected (magenta arrows). Note that the initial apical indentation (red arrowhead) quickly disappeared after stimulation upon relaxation of the cell apex. N = 3 for unstimulated embryos and N = 10 for stimulated embryos. Scale bars: cross-sections, 20 μm; en face views, 10 μm.

Figure 3

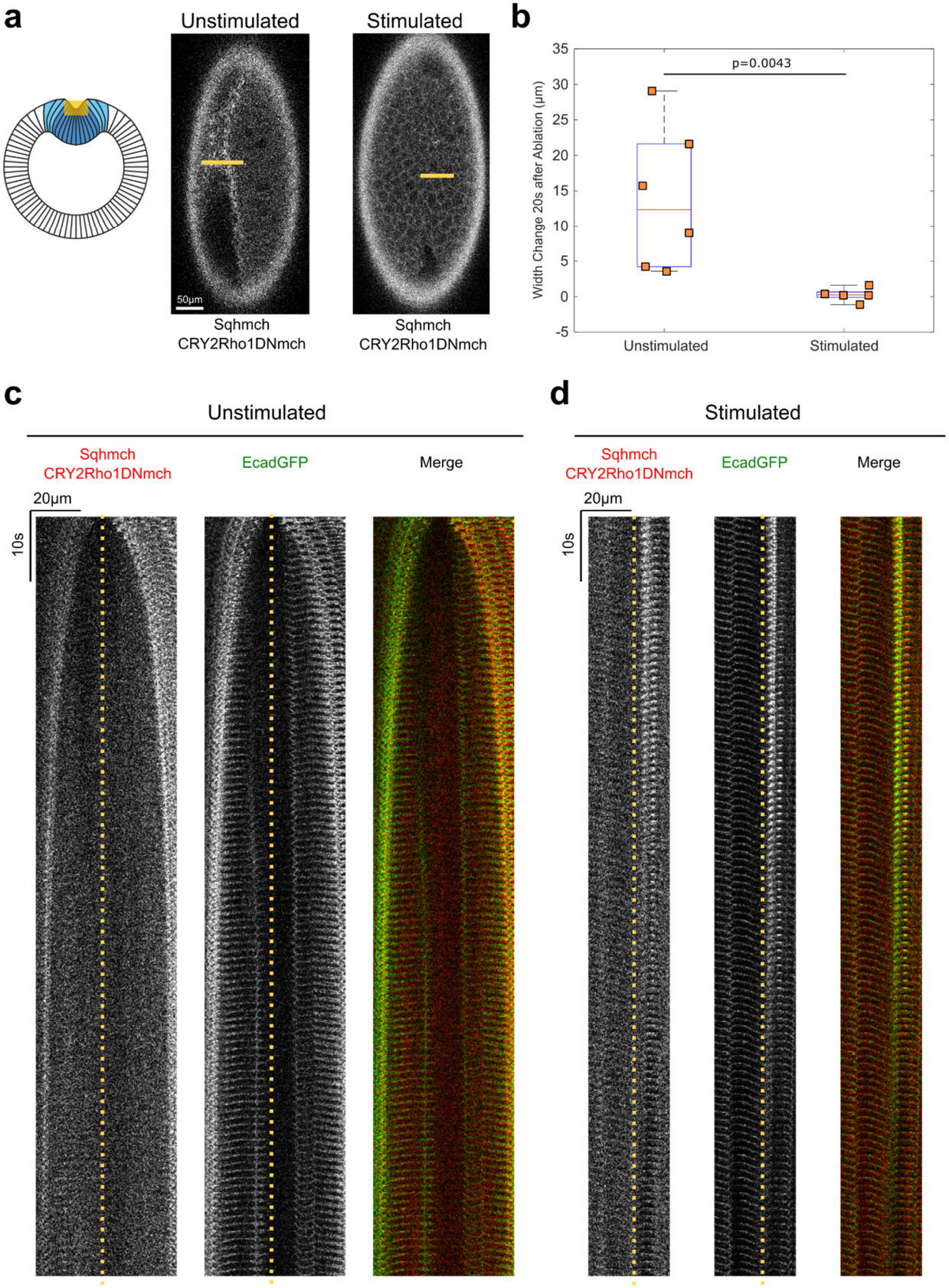
a
Unstimulated
Stimulated
50µm
Sqhmch
CRY2Rho1DNmch
Sqhmch
CRY2Rho1DNmch
b
p=0.0043
Width Change 20s after Ablation (µm)
35
30
25
20
15
10
5
0
-5
Unstimulated
Stimulated
c
Unstimulated
Sqhmch
CRY2Rho1DNmch
EcadGFP
Merge
20µm
10s
d
Stimulated
Sqhmch
CRY2Rho1DNmch
EcadGFP
Merge
20µm
10s

Figure 3. Opto-Rho1DN stimulation during apical constriction results in an immediate loss of cortical tension at ventral surface of the embryo. (a) Cartoon depicting the experimental setup for laser ablation to detect cortical tension. Yellow shaded regions indicate the ablated regions. For stimulated embryos, light-activation of Opto-Rho1DN was performed three minutes before the laser ablation. Due to apical relaxation after stimulation, multiple z-planes were ablated (yellow shaded region) in order to ensure the ablation of the very apical surface of the ventral cells. **(b)** Width changes of the ablated region along the A-P axis during the first 20 seconds after laser ablation. A clear tissue recoil was observed after laser cutting in the unstimulated control embryos. In contrast, little to no tissue recoil was observed in the stimulated embryos, indicating lack of apical tension after Rho1 inhibition. P-value was calculated using two-sided Wilcoxon rank sum test. **(c-d)** Kymographs showing the comparison between unstimulated and stimulated embryos. No obvious tissue recoil was observed in the stimulated embryos (N = 6 for unstimulated embryos and N = 5 for stimulated embryos). Dotted line indicates ablation site.

Figure 4

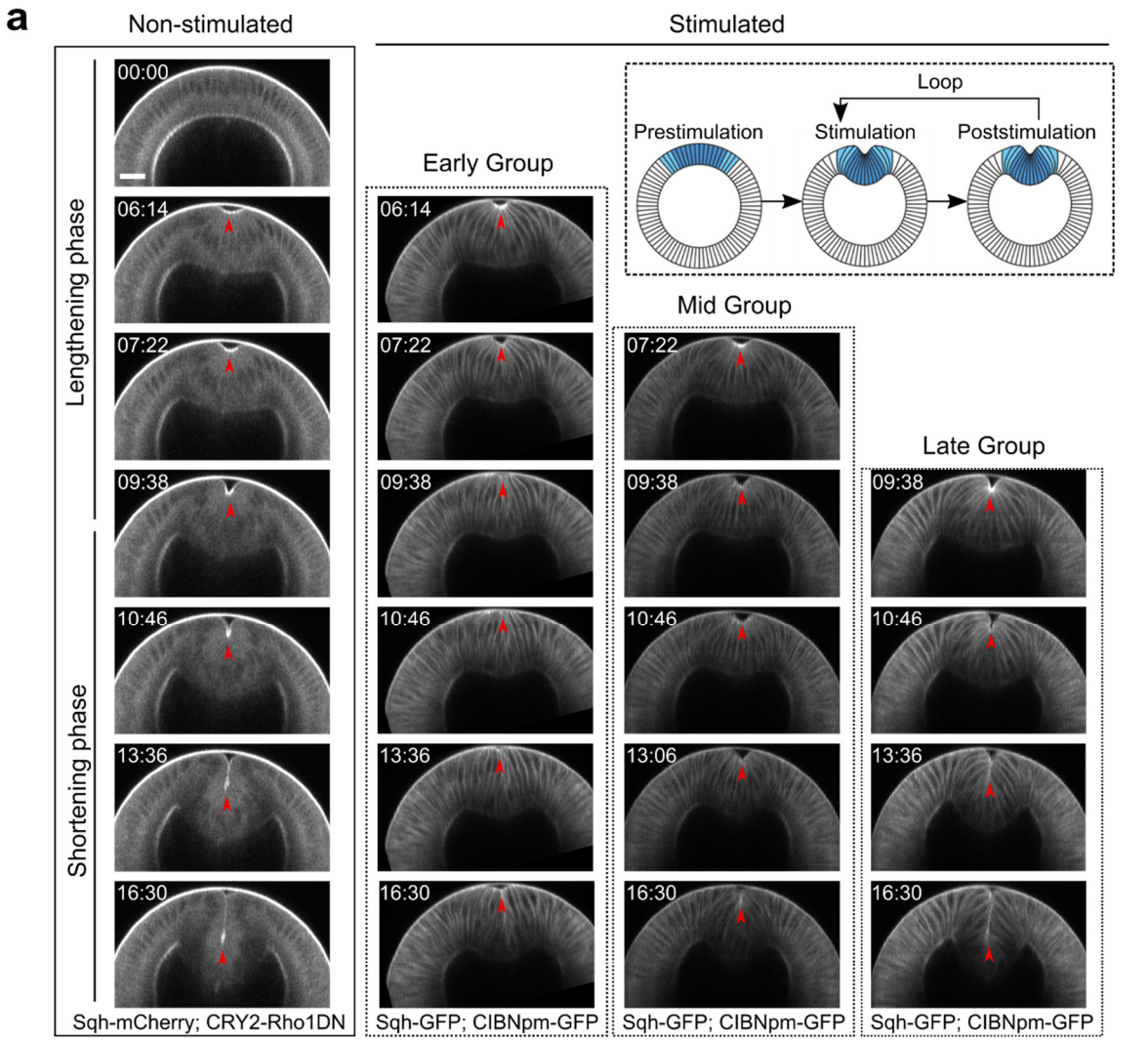
a
Non-stimulated
Stimulated
Lengthening phase
Shortening phase
00:00
06:14
07:22
09:38
10:46
13:36
16:30
Sqh-mCherry; CRY2-Rho1DN
Early Group
Mid Group
Late Group
Sqh-GFP; CIBNpm-GFP
Loop
Prestimulation
Stimulation
Poststimulation

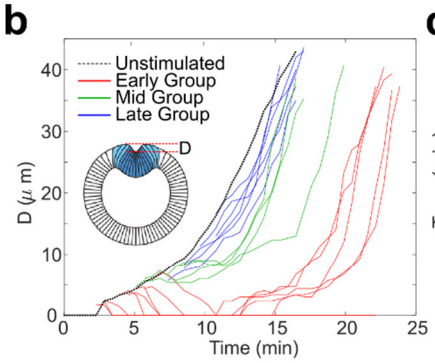
b
Unstimulated
Early Group
Mid Group
Late Group
D
D (μ m)
Time (min)

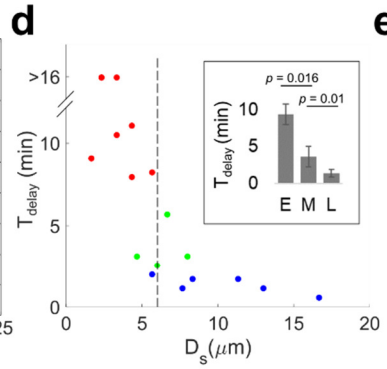
d
p = 0.016
p = 0.01
T_delay (min)
E M L
D_s(μm)

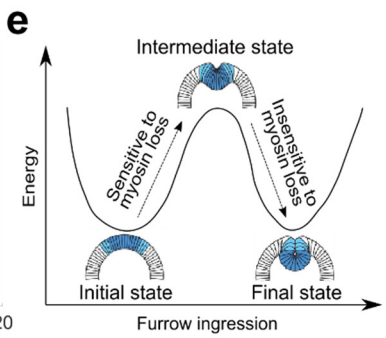
e
Intermediate state
Sensitive to myosin loss
Insensitive to myosin loss
Energy
Initial state
Final state
Furrow ingression

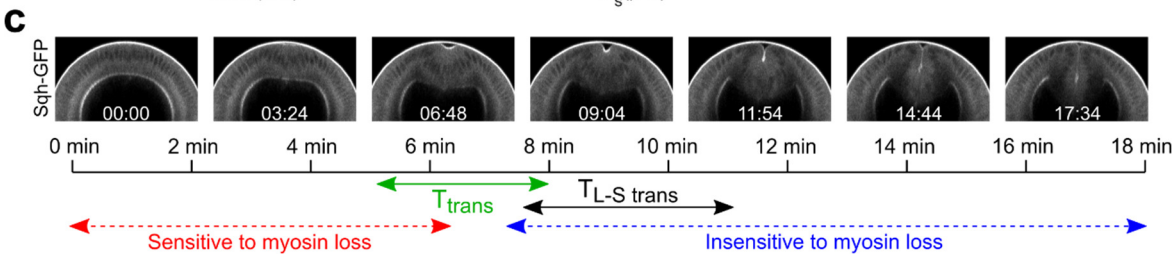
c
Sqh-GFP
00:00
03:24
06:48
09:04
11:54
14:44
17:34
0 min
2 min
4 min
6 min
8 min
10 min
12 min
14 min
16 min
18 min
T_trans
T_L-S trans
Sensitive to myosin loss
Insensitive to myosin loss

Figure 4. Acute inhibition of actomyosin contractility results in stage dependent response during ventral furrow formation. (a) Still images from multiphoton movies showing different tissue responses to acute loss of myosin contractility during ventral furrow formation. Early Group, Mid Group and Late Group embryos (N = 8, 4, and 6 embryos, respectively) are defined based on their immediate response to myosin inhibition. For stimulated embryos, the first frame corresponds to the time point immediately after stimulation. The inset depicts the stimulation and imaging protocol. Arrowheads indicate the apex of the ventral most cells. **(b)** Time evolution of the invagination depth "D" for the stimulated embryos and a representative unstimulated control embryo. For stimulated embryos, all movies were aligned in time to the representative control embryo based on furrow morphology at the time of stimulation. **(c)** Relationship between the transition phase for sensitivity to myosin inhibition (T_{trans}) and lengthening-shortening transition ($T_{L\text{-}S\ trans}$). **(d)** Scatter plot showing the relation between invagination depth at the time of stimulation (D_s) and the delay time (T_{delay}) in furrow invagination compared to the representative control embryo. T_{delay} is highly sensitive to D_s, with a switch-like change at $D_s \sim 6$ μm (dashed line). Inset: Average T_{delay} in Early (E, n = 5 embryos that invaginated), Mid (M, n = 4) and Late (L, n = 6) Group embryos. Statistical comparisons were performed using two-sided Wilcoxon rank sum test. **(e)** Cartoon depicting mechanical bistability of the mesoderm during gastrulation. Both the initial, pre-constriction state and the final, fully invaginated state are stable. During gastrulation, actomyosin contractility is critical for bringing the system from the initial state to an intermediate, transitional state, whereas the subsequent transition to the final state can occur independent of myosin contractility.

Figure 4 - figure supplement 1

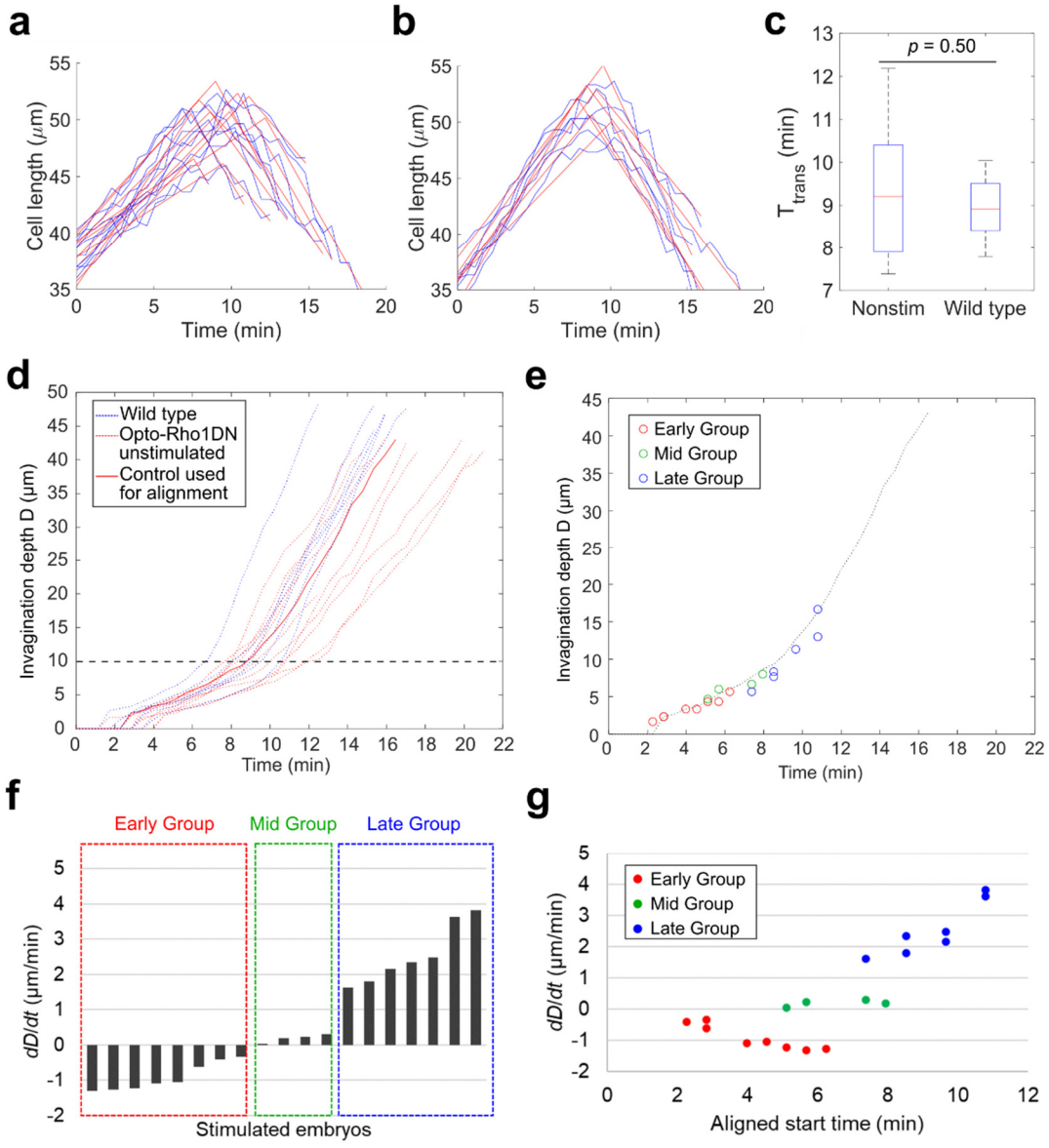

Figure 4 – figure supplement 1. Classification of the response of embryos to acute myosin inhibition during ventral furrow formation. (a-c) Determining the transition point between the lengthening and shortening phases ($T_{L\text{-}S\ trans}$). (a, b) Measurement of apical-basal cell length of the ventral most cells over the course of ventral furrow formation in unstimulated control embryos that express Opto-Rho1DN (a, unstimulated control, N = 10) and wildtype embryos that do not express Opto-Rho1DN (b, wild type, N = 6). For each group, one obvious outlier was excluded from the analysis. The raw measurement for each embryo (blue) is fitted with two intersecting line segments (red) to determine $T_{L\text{-}S\ trans}$. The distribution of $T_{L\text{-}S\ trans}$ for unstimulated control embryos and wild type embryos is shown in **(c)**. There is no significant difference between the two control groups (Student's t-test). Error bars: s.d. **(d)** Measurement of invagination depth D in unstimulated control embryos (red dotted lines) and wildtype embryos (blue dotted lines). Red solid line marks the representative unstimulated control embryo used for time alignment of the stimulated embryos. Black dashed line indicates the average invagination depth at $T_{L\text{-}S\ trans}$. **(e)** Alignment of the stimulated embryos to the representative control embryo (dotted line) based on furrow morphology immediately before stimulation. Each open circle shows the invagination depth D of a stimulated embryo at the aligned starting time. **(f)** The average rate of invagination within the first 4 minutes immediately after stimulation (dD/dt) is used to categorize the stimulated embryos into three groups. Early Group: $dD/dt < -0.3$ μm/min; Mid Group: dD/dt is between -0.3 μm/min and 0.3 μm/min; Late Group: $dD/dt > 0.3$ μm/min. **(g)** dD/dt as a function of aligned starting time as defined in **(e)**. Note that there is no positive correlation between dD/dt and the stage of stimulation among Early Group or Mid Group embryos.

Figure 4 - figure supplement 2

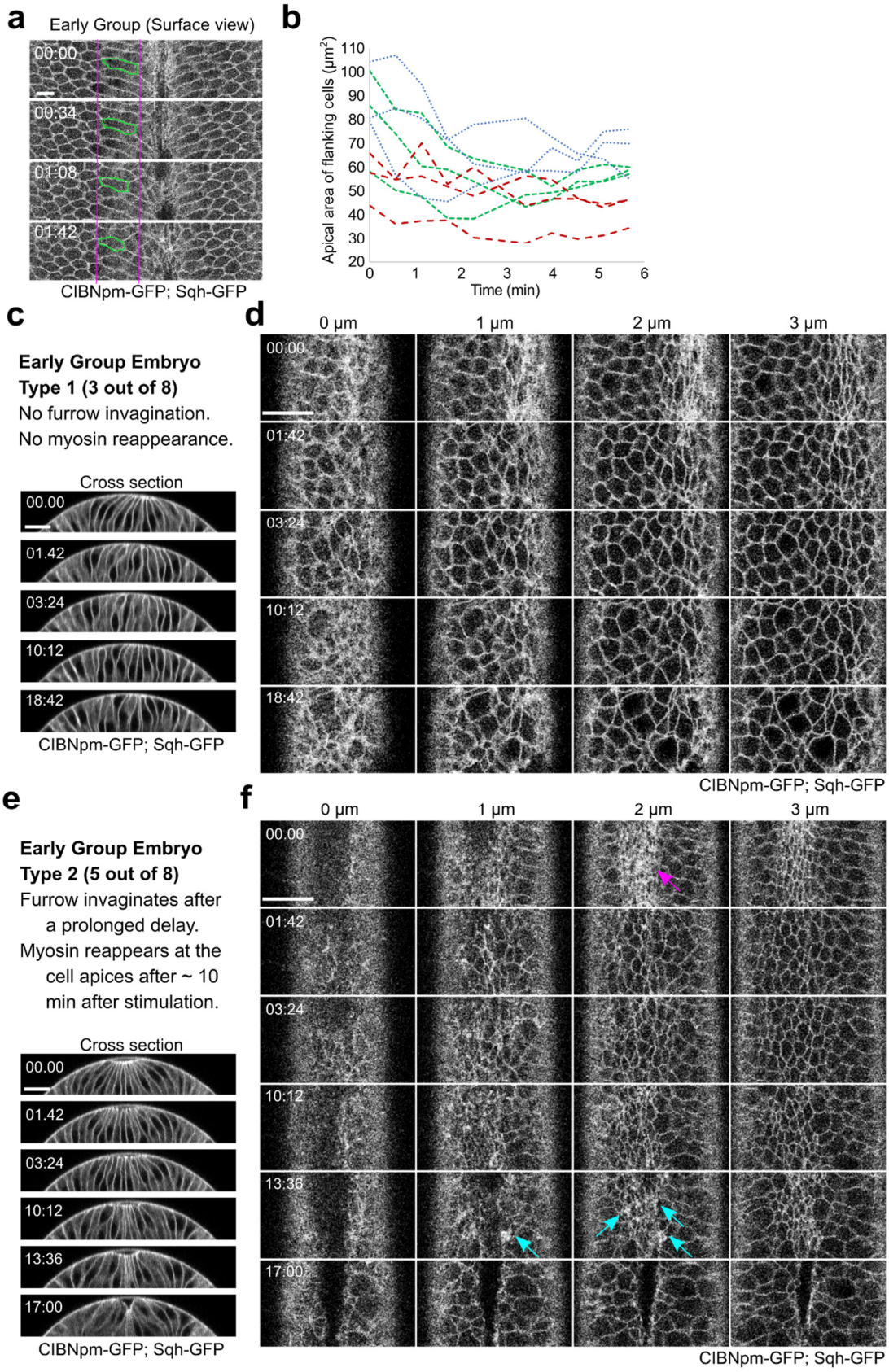

Figure 4 – figure supplement 2. Tissue response to acute myosin inhibition in Early Group embryos. (a) Surface view of a representative Early Group embryo showing elastic recoil of apical domain of the flanking non-constricting cells upon activation of Opto-Rho1DN. During apical constriction, the apical domain of the flanking non-constricting cells is stretched by the ventral constricting cells. Upon myosin inhibition, the stretched apical domain relaxes back. One example cell is marked in green. Scale bar: 10 μm. **(b)** Quantification of apical domain size of the flanking non-constricting cells in three Early Group embryos after stimulation, with three cells measured in each embryo. **(c, d)** A representative Early Group embryo that remains at the non-constricted configuration after apical relaxation (Early Group Type 1, 3 out of 8 embryos). Images show a combined signal from CIBNpm-GFP (cell membrane) and Sqh-GFP (medial apical). After the initial relaxation of the apical domain, the apical cell area becomes progressively heterogeneous, but no net apical constriction occurs. Ventral cells remain at the surface of the embryo without forming a furrow. **(e, f)** A representative Early Group embryo that undergoes ventral furrow invagination after a prolonged delay (Early Group Type 2, 5 out of 8 embryos). In these embryos, Sqh-GFP partially reaccumulates at the cell apices, which becomes obvious approximately ten minutes after the first stimulation (cyan arrows in f). The reaccumulated myosin has a lower level and more heterogeneous distribution compared to the same embryo before stimulation (magenta arrow in f). Nevertheless, accompanying with the reaccumulation of apical myosin, the ventral cells invaginate and form a ventral furrow. Scale bars: 20 μm. In all panels, time zero corresponds to the time of first stimulation.

Figure 4 - figure supplement 3

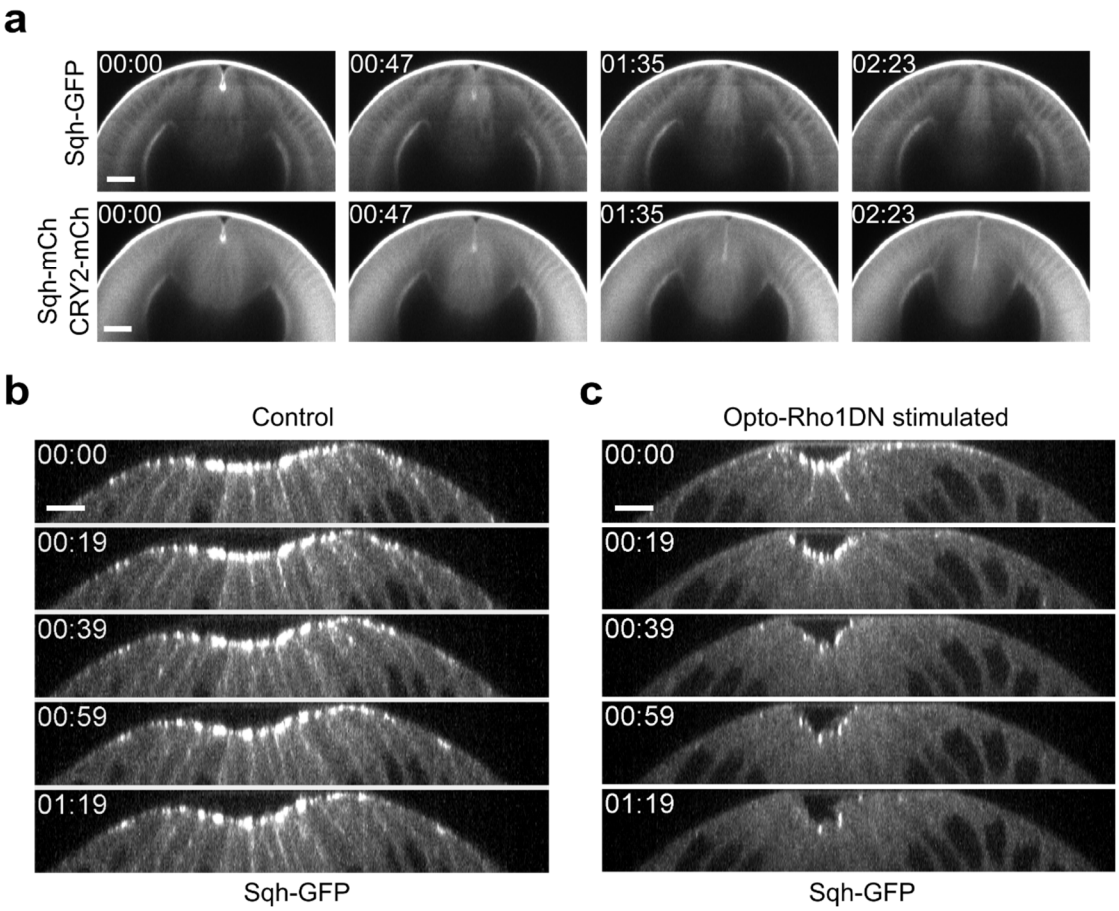

Figure 4 – figure supplement 3. Dissociation of myosin from both apical and lateral cell cortices in constricting cells upon Opto-Rho1DN stimulation. (a) Cross section views of a representative Late Group embryo showing prompt dissociation of apical myosin from the apical cortex (N = 4 embryos). The embryo expresses CIBNpm instead of CIBNpm-GFP to allow better visualization of Sqh-GFP. Sqh-GFP is accumulated at the apical cortices before stimulation but disappears from the apical cortices in less than 1.6 min. Sqh-mCherry and mCherry-tagged CRY2-Rho1DN signals in the same embryo is shown at the lower panel for comparison. Time zero corresponds to the time of stimulation. Scale bars: 20 μm. **(b, c)** Cross-section views of a control embryo expressing Sqh-GFP and CIBNpm (b) and an embryo expressing Sqh-GFP, CIBNpm and CRY2- Rho1DN (c). In control embryos, lateral myosin appears during apical constriction and can always be detected as constriction proceeds (N = 8 embryos). In contrast, in embryos expressing Opto-Rho1DN, lateral myosin disappears within 20 seconds after stimulation, faster than the loss of apical myosin (N = 6 embryos). Scale bars: 10 μm.

Figure 5

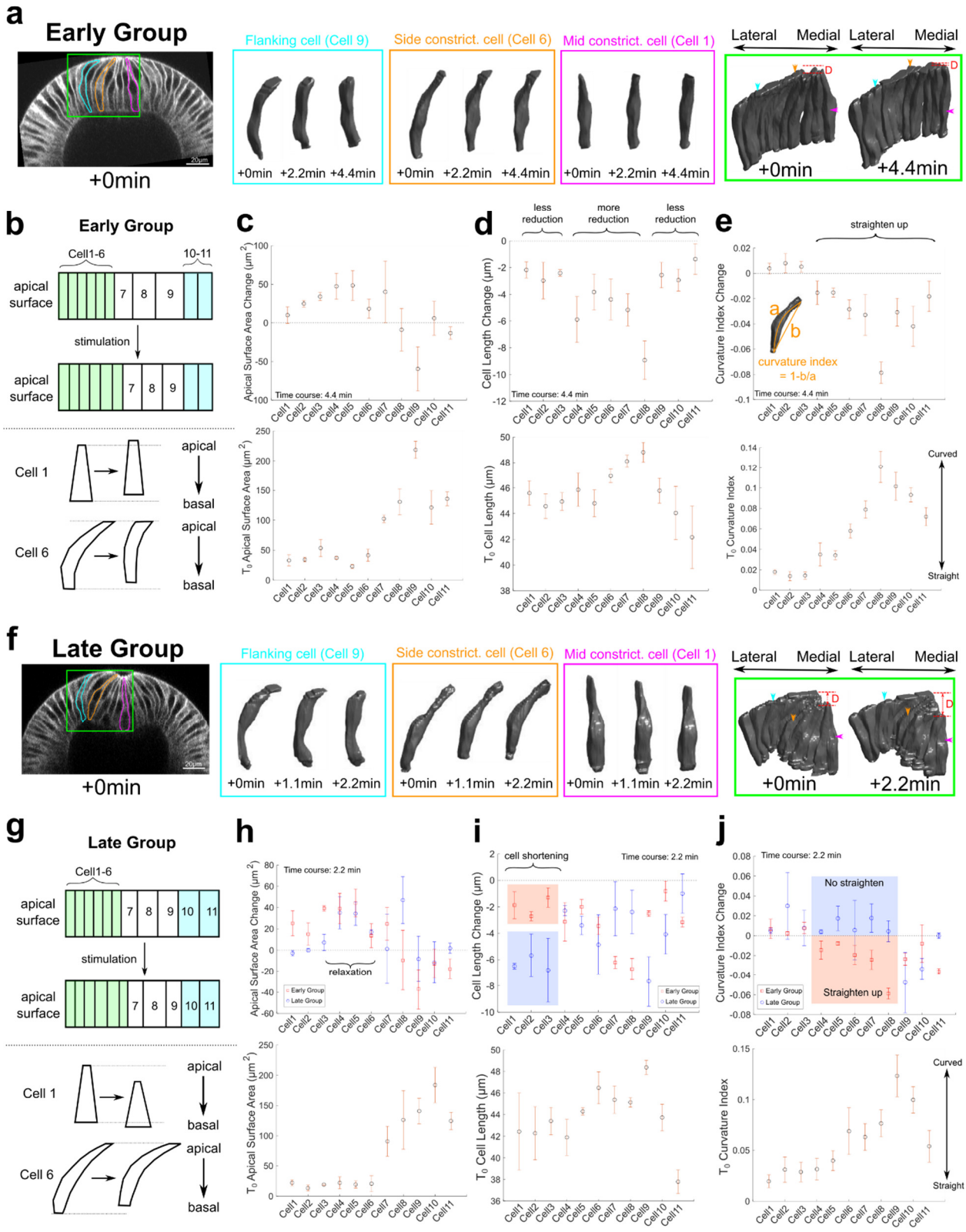
a
Early Group
+0min
Flanking cell (Cell 9)
Side constrict. cell (Cell 6)
Mid constrict. cell (Cell 1)
+0min +2.2min +4.4min
Lateral Medial Lateral Medial
+0min
+4.4min
b
Early Group
Cell1-6
10-11
apical surface
stimulation
Cell 1
Cell 6
apical
basal
c
Apical Surface Area Change (μm²)
Time course: 4.4 min
T0 Apical Surface Area (μm²)
d
less reduction
more reduction
less reduction
Cell Length Change (μm)
T0 Cell Length (μm)
e
straighten up
Curvature Index Change
curvature index = 1-b/a
T0 Curvature Index
Curved
Straight
f
Late Group
+0min
Flanking cell (Cell 9)
Side constrict. cell (Cell 6)
Mid constrict. cell (Cell 1)
+0min +1.1min +2.2min
Lateral Medial Lateral Medial
+0min
+2.2min
g
Late Group
Cell1-6
h
Time course: 2.2 min
relaxation
Early Group
Late Group
i
cell shortening
j
No straighten
Straighten up

Figure 5. Three-dimensional segmentation reveals details of cell response after Opto-Rho1DN stimulation. (a-e) Early Group embryos and **(f-j)** Late Group embryos. **(a, f)** A row of cells along the medial-lateral axis on one side of the ventral midline was segmented in 3D (green box) over time after stimulation. Cell 1 – 6: constricting cells; Cell 7 – 9: flanking cells; Cell 10 – 11: ectodermal cells. Early Group: T = 0, 2.2, and 4.4 minutes. Late Group: T = 0, 1.1, and 2.2 minutes. 3D rendering of three representative cells, cell 1 (mid constricting cell), cell 6 (side constricting cell) and cell 9 (flanking cell), are shown in magenta, orange and cyan boxes, respectively. These cells are also marked on the cross-section views (outlines) and the 3D tissue renderings (arrowheads) with the same color code. D: invagination depth. **(b, g)** Cartoon depicting apical surface area change (top) and characteristic cell shape changes (bottom) observed in Early Group (b) and Late Group (g) embryos. **(c-e, h-j)** Upper panels: quantifications showing the apical surface area change (c, h), cell length change (d, i) and cell curvature change (e, j) between 0 and 4.4 minutes (c-e) or between 0 and 2.2 minutes (h-j). Measurements from both Early and Late Groups are shown in h-j for comparison. Bottom panels show the measurements for each quantity immediately after stimulation (T = 0). Error bars: ± s.e. N = 3 embryos for each group.

Figure 5 - figure supplement 1

a Early Group at 4.4min after stimulation

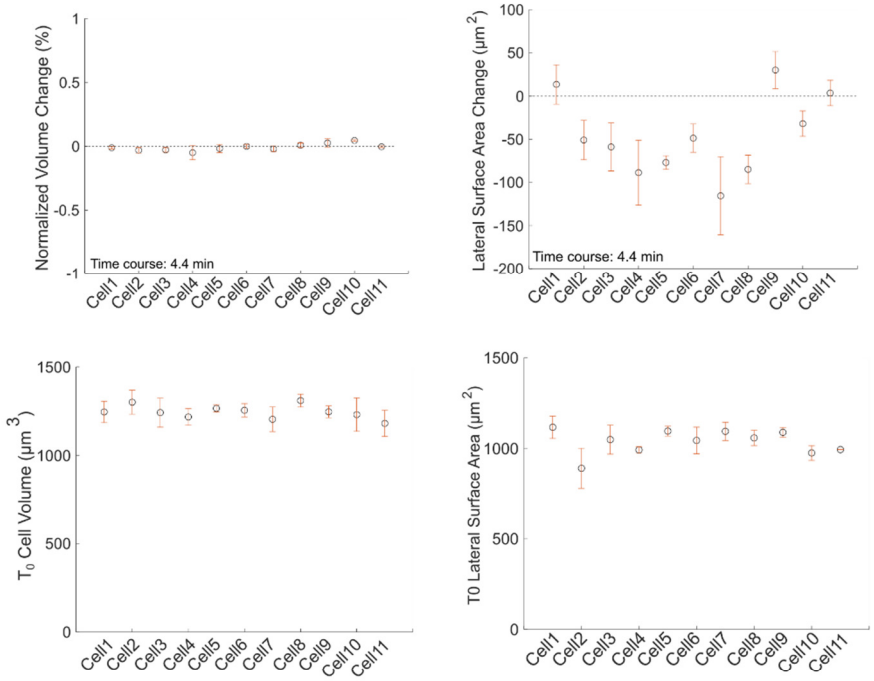

b Early and Late Group at 2.2min after stimulation

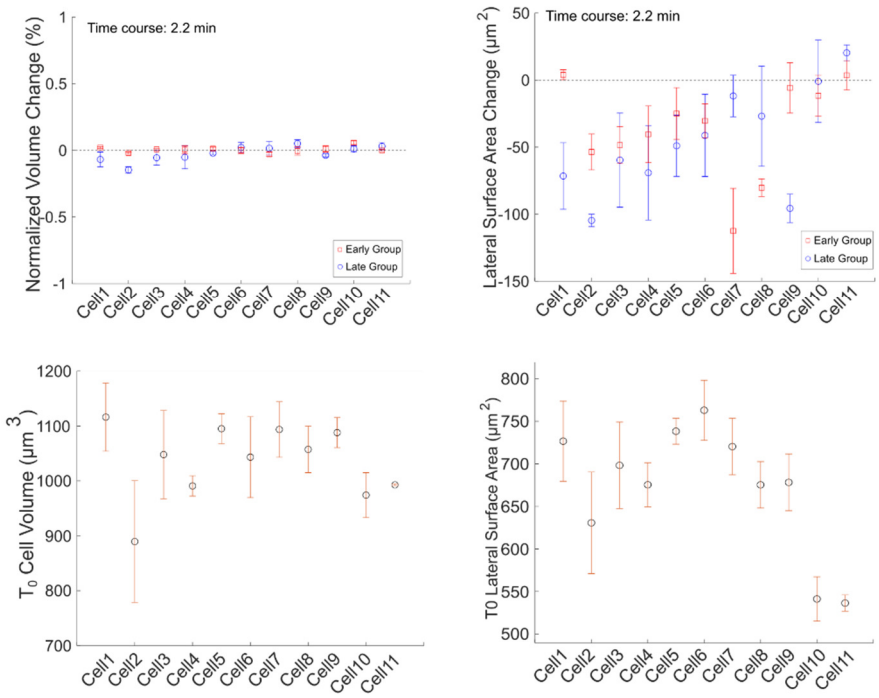

Figure 5 – figure supplement 1. Volume conservation and lateral surface change in Early (a) and Late (b) Group embryos after Opto-Rho1DN stimulation. Top panels: Volume change and lateral surface change between 0 and 4.4 minutes or between 0 and 2.2 minutes after stimulation. Measurements from both Early and Late Groups are shown in (b) for comparison. Bottom panels: Initial volume and lateral surface area immediately after stimulation (T = 0) in both groups. The change of volume is normalized to the initial cell volume at T = 0.

Figure 6

a

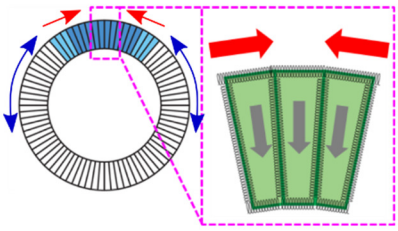

Apical constriction
Compressive stress

Modified from Polyakov et al., 2014

b

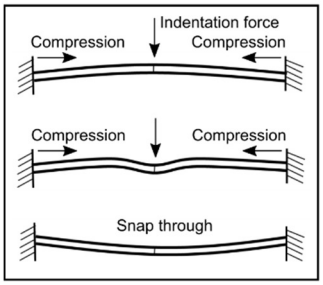

Modified from Qiu et al., 2004

c

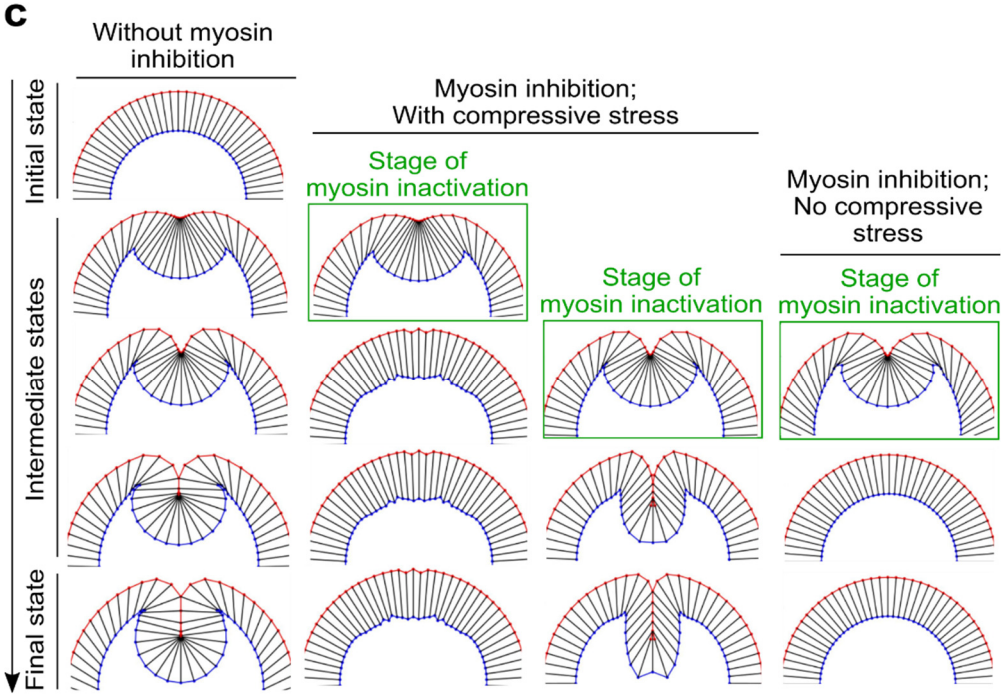

d

Final equilibrium configuration

	No compressive stress	With compressive stress
6 constricting cells (50% of WT)	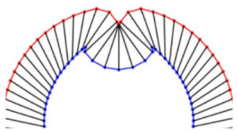	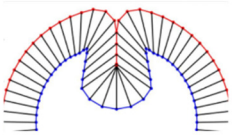
Constriction in every other cell	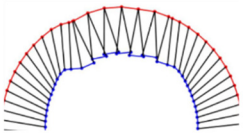	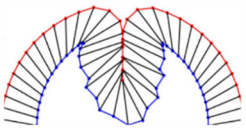

Figure 6. Mechanical bistability of the mesoderm during gastrulation can arise from ectoderm-derived compressive stresses. (a) 2D vertex model testing the mechanisms of mechanical bistability of the mesoderm during gastrulation. In this model, the apical, lateral and basal cortices of cells are modeled as elastic springs that resist deformations, the cell interiors are non-compressible, and the only two active energy inputs are apical constriction in the mesoderm (blue cells) and in-plane compression generated by the ectoderm (white cells). **(b)** Buckling of a compressed elastic beam triggered by a transverse indentation force. **(c)** The model recapitulates the bipartite response to acute loss of actomyosin contractility only when the in-plane compression is present. Column 1 shows normal ventral furrow formation. Column 2 – 4 show tissue response when apical constriction is inhibited at different stages of ventral furrow formation with or without ectodermal compression. **(d)** Model predictions on the impact of reducing the width of apical constriction domain or the uniformity of apical constriction on final invagination depth. In the presence of compressive stress, final invagination depth becomes less sensitive to perturbations of apical constriction.

Figure 6 - figure supplement 1

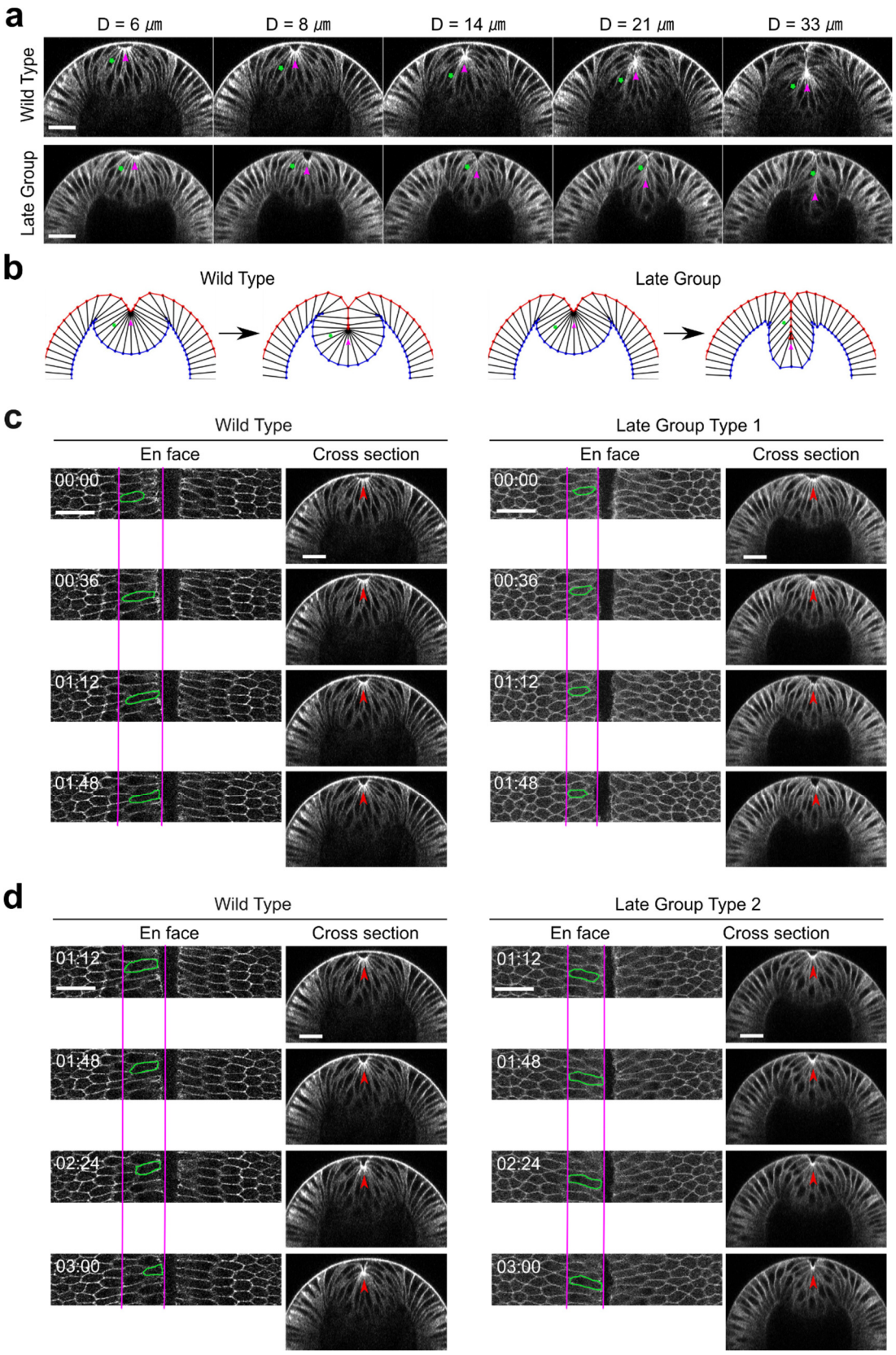

Figure 6 – figure supplement 1. Myosin inhibition in Late Group embryos results in fewer cells incorporated into the ventral furrow. (a) Selected constricting cells (green stars) located near the boundary of the apical constriction domain are tracked over time in a wildtype embryo and a Late Group embryo. Magenta arrowheads indicate the apex of the ventral most cells. In both embryos, the tracked cells start at similar location. However, in the fully invaginated configuration, the cell in the Late Group embryo is located closer to the surface of the embryo compared to that in the wildtype embryo, suggesting that fewer cells are incorporated into the furrow (N = 6). Note that the reduction in the number of cells incorporated into the furrow does not affect the rate of D increase over time. Scale bars: 25 μm. **(b)** The phenotype in furrow morphology is well recapitulated in the simulated Late Group embryo presented in Figure 3. **(c, d)** Behavior of the flanking non-constricting cells in Late Group embryos. Representative cells are outlined in green. Red arrowheads indicate the apex of the ventral most cells. (c) After stimulation, the flanking cells in Late Group embryos that have shallower D_s (i.e. embryos that just pass T_{trans}; Late Group Type 1, N = 2 embryos) show mild apical retraction. For comparison, in the stage matched wildtype embryos, the flanking cells continue to move ventrally. (d) After stimulation, the flanking cells in Late Group embryos with deeper D_s (i.e., embryos that are more advanced in the invagination process, Late Group Type 2, N = 4 embryos) show no apical relaxation, but their ventral movement is slower than those in the stage matched wildtype embryos. Despite these differences, the rate of furrow invagination is comparable between Late Group embryos and the wildtype embryos. Scale bars: 25 μm.

Figure 7

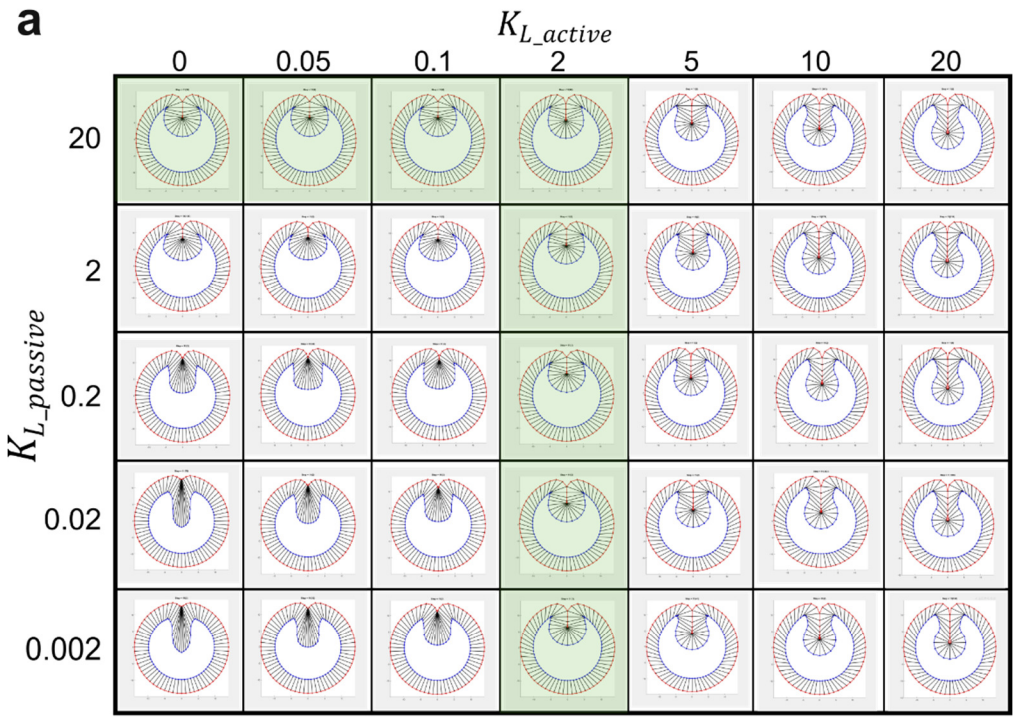
a
K_{L_active}
0
0.05
0.1
2
5
10
20
$K_{L_passive}$
20
2
0.2
0.02
0.002

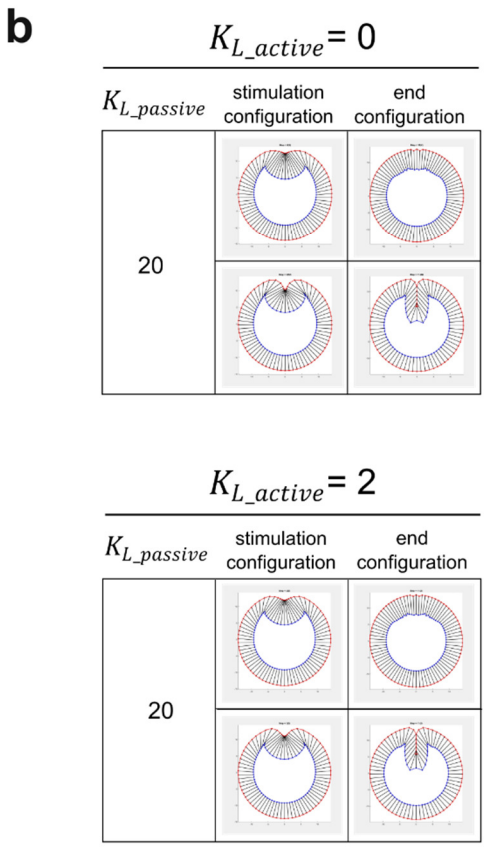
b
K_{L_active}= 0
$K_{L_passive}$
stimulation configuration
end configuration
20
K_{L_active}= 2
$K_{L_passive}$
stimulation configuration
end configuration
20

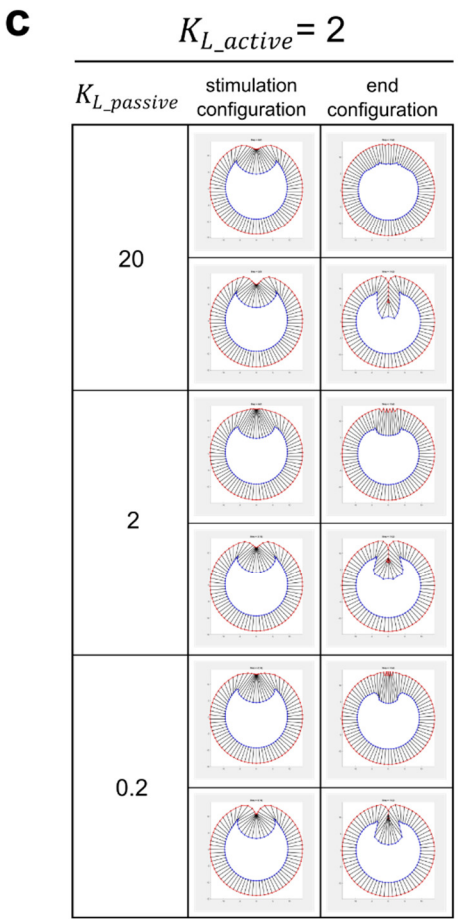
c
K_{L_active}= 2
$K_{L_passive}$
stimulation configuration
end configuration
20
2
0.2

Figure 7. Modeling analysis of the impact of myosin-dependent and myosin-independent cell shortening force in the constriction domain on binary tissue response. (a) The myosin-dependent, active lateral shortening force and myosin-independent, passive lateral shortening forces function additively to mediate cell shortening and furrow invagination in the 2D vertex model. The active and passive lateral forces are given by $K_{L_active}l$ and $K_{L_passive}(l - l_0)$, respectively, where l and l_0 are the current and the resting length of the lateral edge, respectively. Green shaded region represents the conditions where the model generates normal final furrow morphology. **(b)** When $K_{L_passive} = 20$, changing K_{L_active} has little impact on the binary response of the model to stimulation. **(c)** When $K_{L_active} = 2$, changing $K_{L_passive}$ does not affect the binary tissue response per se but influences the final morphology after stimulation.

Figure 8

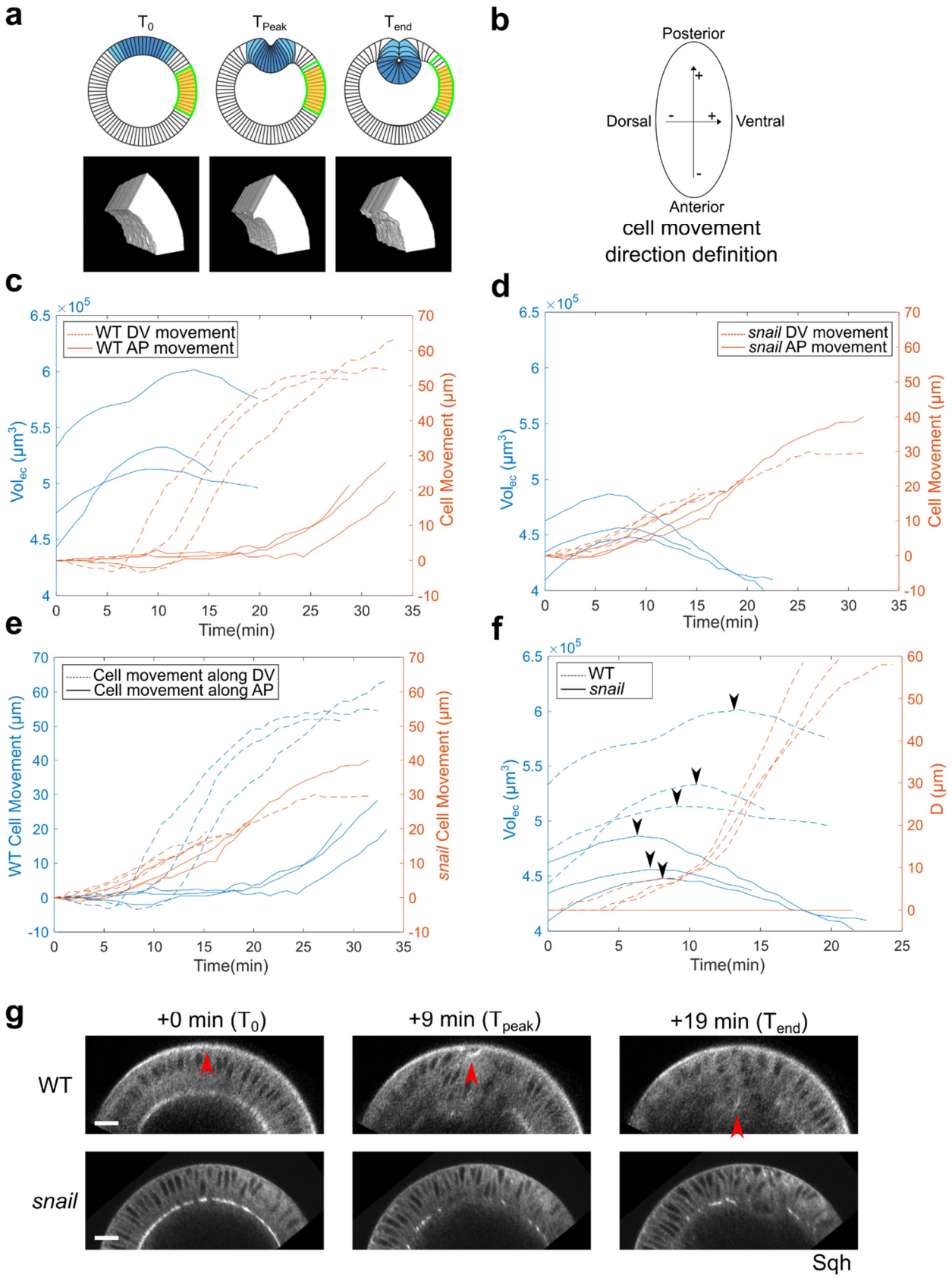
a
T0
TPeak
Tend
b
Posterior
Dorsal
Ventral
Anterior
cell movement direction definition
c
WT DV movement
WT AP movement
Volec (µm3)
Cell Movement (µm)
Time(min)
d
snail DV movement
snail AP movement
Volec (µm3)
Cell Movement (µm)
Time(min)
e
Cell movement along DV
Cell movement along AP
WT Cell Movement (µm)
snail Cell Movement (µm)
Time(min)
f
WT
snail
Volec (µm3)
D (µm)
Time(min)
g
+0 min (T0)
+9 min (Tpeak)
+19 min (Tend)
WT
snail
Sqh

Figure 8. The lateral ectoderm undergoes apical-basal shortening during gastrulation independently of ventral furrow formation. (a) Top: Cartoon showing a cross-section view of an embryo. Blue: mesoderm. Yellow: segmented ectoderm region ("ROI"). Green: the same group of ectoderm cells. The ROI (in 3D) covers the lateral ectodermal region that is 60-120 degree away from the ventral midline and 75 μm long along the AP axis. The change in the volume of ROI ("Vol_{ec}") is used as a readout for change in average tissue thickness. Bottom: representative segmented 3D views showing the ectoderm at the onset of apical constriction (T_0), reaches the thickest point (T_{peak}) and at the last time frame of ventral furrow formation that is reliably segmented (T_{end}). **(b)** Definition for the direction of cell movement used in (c-f). **(c-d)** Change in Vol_{ec} over time and cell movement along A-P and D-V axis in wildtype (c) and *snail* mutant embryos (d). **(e)** Cell movement along A-P and D-V axis in wildtype and *snail* mutants are replotted together for better comparison. **(f)** Change in Vol_{ec} and invagination depth D over time in wildtype and *snail* mutant embryos. Arrowheads indicate the start of ectoderm shortening. **(g)** Representative cross-section views showing the wildtype and *snail* mutant embryos at T_0, T_{peak}, and T_{end}, respectively. Arrowheads indicate the apex of the mid constricting cells. N = 3 embryos for each genotype. Scale bars: 20 μm.

Figure 8 - figure supplement 1

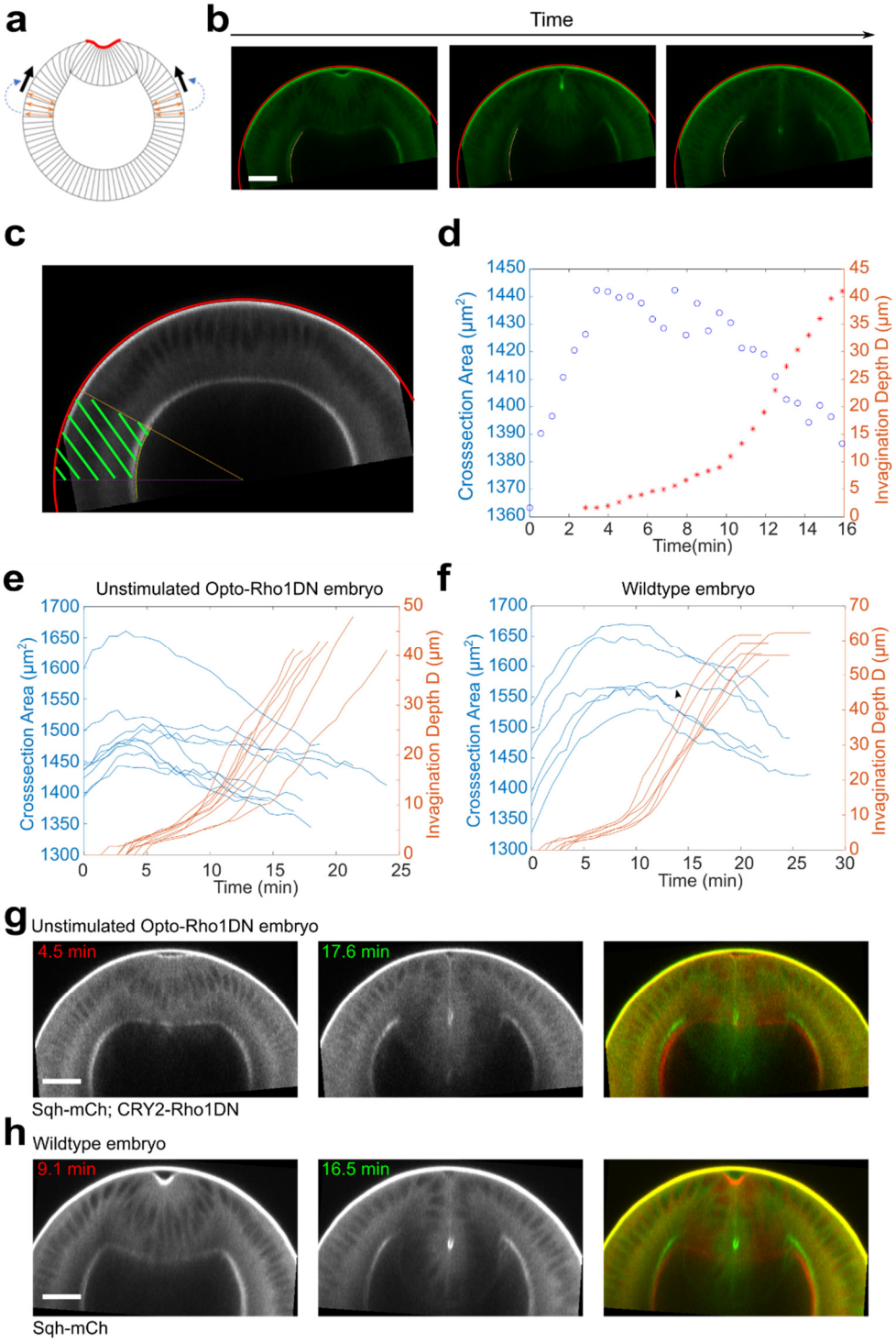

Figure 8 – figure supplement 1. Lateral ectoderm undergoes apical-basal shortening during ventral furrow formation. (a) Cartoon depicting a possible link between ectodermal shortening and the generation of compressive stress. Because the cytoplasm is non-compressible, apical basal shortening of the ectodermal cells could lead to cell expansion in the planar direction, thereby generating in-plane compression that facilitates mesoderm invagination. **(b)** Images show the tracked apical (red) and basal (yellow) surfaces of the lateral ectoderm during furrow formation. **(c)** The ectodermal region in the cross-section view between 60 and 90 degrees from the ventral midline was selected for area measurement ("Cross-section area", green shaded region). **(d)** Relationship between ectodermal tissue area and invagination depth D in a representative unstimulated Opto-Rho1DN embryo. Ectodermal tissue shortening happens prior to $T_{L\text{-}S\ trans}$. T = 0 min represents the onset of apical constriction. **(e, f)** Time evolution of the invagination depth D (orange lines) and the cross-section area of the lateral ectodermal tissue (blue lines) measured in unstimulated Opto-Rho1DN embryos (e, N = 9 embryos) and in wildtype embryos expressing Ecad-GFP and Sqh-mCherry (f, N = 6 embryos). In unstimulated Opto-Rho1DN embryos, the onset of ectodermal shortening is consistently earlier than $T_{L\text{-}S\ trans}$. A similar trend is observed in most (5 out of 6) wildtype embryos, although the onset of ectodermal shortening was overall closer to $T_{L\text{-}S\ trans}$ in this background. In one out of six wildtype embryos, ectodermal shortening only became obvious at a late stage of furrow invagination (arrowhead in f). **(g, h)** Cross-section views of representative unstimulated Opto-Rho1DN embryo (g) and wildtype embryo (h) at early and late stages of furrow formation. Overlayed images highlight the reduction of ectodermal thickness. Scale bars: 25 μm.

Figure 8 - figure supplement 2

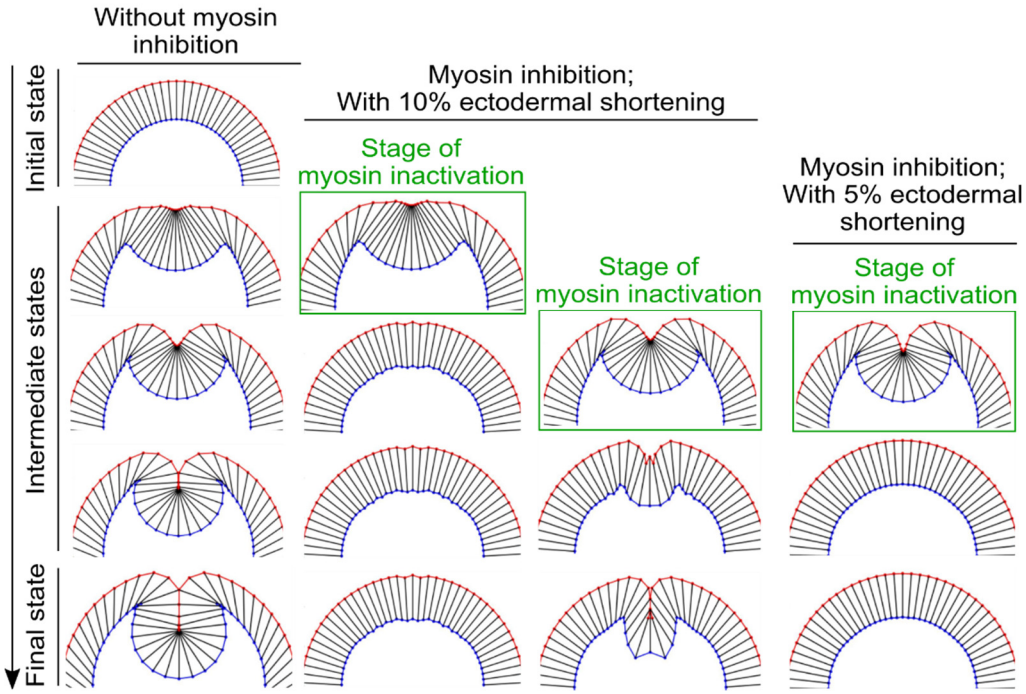

Figure 8 – figure supplement 2. The impact of altering the extent of ectodermal shortening on the response of the model to acute myosin inhibition. When the percent reduction of the ectodermal cell length is lowered from 20% to 10%, the binary response to acute myosin inhibition is still present, although the final depth of the furrow in the simulated Late Group embryo is reduced. Further lowering the percent reduction of the ectodermal cell length to 5% abolishes the binary response – in this case, the intermediate furrow always relaxes back to the surface of the embryo after myosin inhibition regardless of the stage of stimulation.

Figure 9

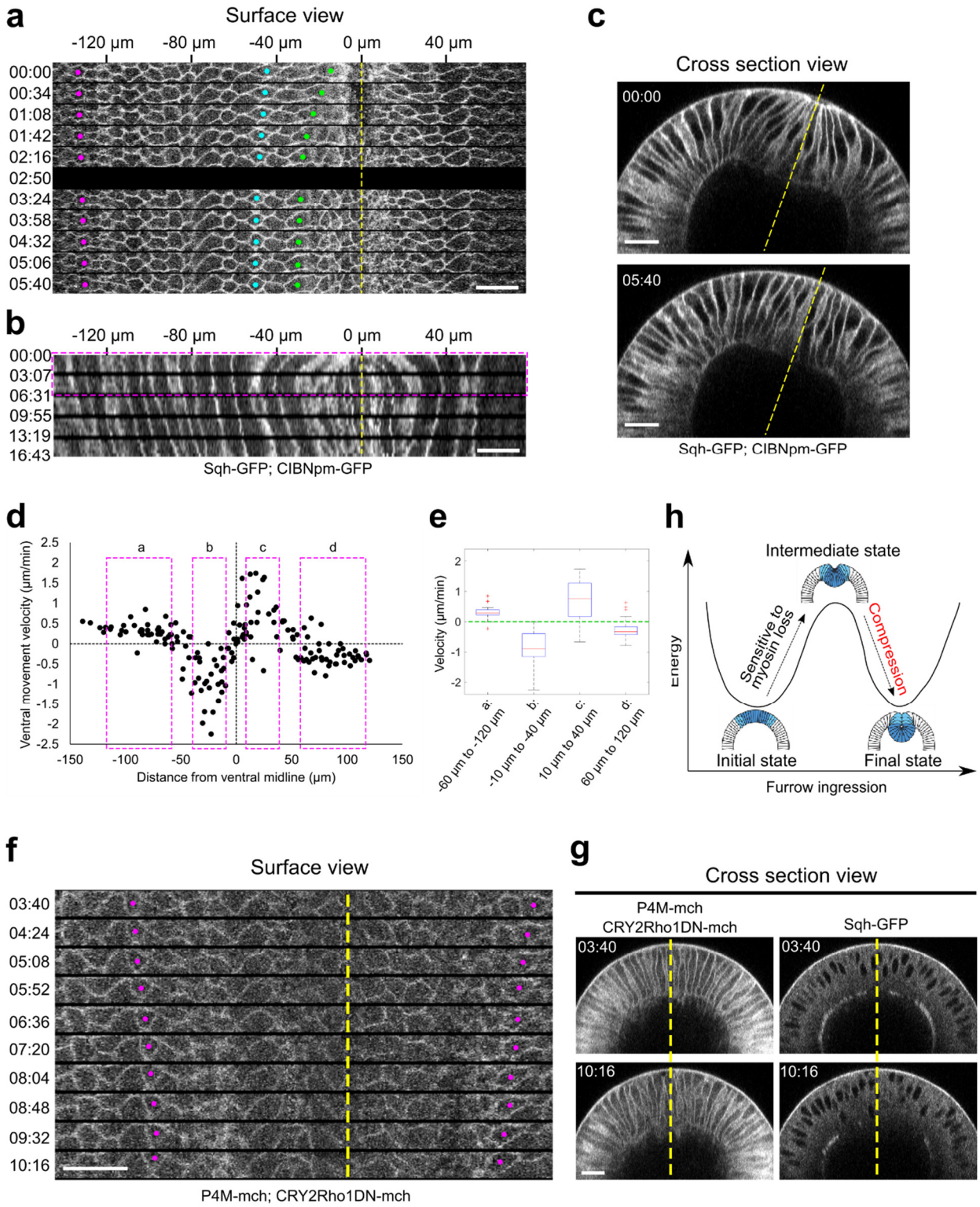
a
Surface view
-120 µm
-80 µm
-40 µm
0 µm
40 µm
00:00
00:34
01:08
01:42
02:16
02:50
03:24
03:58
04:32
05:06
05:40
b
-120 µm
-80 µm
-40 µm
0 µm
40 µm
00:00
03:07
06:31
09:55
13:19
16:43
Sqh-GFP; CIBNpm-GFP
c
Cross section view
00:00
05:40
Sqh-GFP; CIBNpm-GFP
d
Ventral movement velocity (µm/min)
Distance from ventral midline (µm)
a
b
c
d
e
Velocity (µm/min)
a: -60 µm to -120 µm
b: -10 µm to -40 µm
c: 10 µm to 40 µm
d: 60 µm to 120 µm
h
Intermediate state
Energy
Sensitive to myosin loss
Compression
Initial state
Final state
Furrow ingression
f
Surface view
03:40
04:24
05:08
05:52
06:36
07:20
08:04
08:48
09:32
10:16
P4M-mch; CRY2Rho1DN-mch
g
Cross section view
P4M-mch
CRY2Rho1DN-mch
Sqh-GFP
03:40
03:40
10:16
10:16

Figure 9. Lateral ectodermal cells still move ventrally in Early Group embryos when the ventral cells undergo apical relaxation upon Opto-Rho1DN stimulation. (a) Montage showing the surface view of an Early Group embryo during the first six minutes after stimulation (T = 0). Yellow dashed line depicts ventral midline. Despite the tissue relaxation in the ventral region of the embryo (green and cyan dots), the ectodermal cells continue to move towards the ventral midline. **(b)** Kymograph generated from the surface view of the same movie as shown in (a). Magenta box indicates the time window where the average velocity of tissue movement is measured. **(c)** Cross section view of the same embryo in (a) showing the relaxation of the apical indentation at the ventral side of the embryo. Yellow line: DV axis. **(d)** Velocity of tissue movement as a function of the initial distance from the ventral midline. N = 7 Early Group embryos. **(e)** Box plot showing the velocity of tissue movement at ventral mesodermal (b: from -10 to -40 μm, and c: from 10 to 40 μm) or lateral ectodermal (a: from -60 to -120 μm, and d: from 60 to 120 μm) regions of the embryo. Statistical analysis testing whether the measured velocities are significantly larger (a and c) or smaller (b and d) than zero is performed using one-tailed one-sample t-test against 0. $p < 0.001$ for all tests. **(f, g)** Surface kymograph (g) and cross-section views (h) of embryos expressing Opto-Rho1DN and stimulated at the onset of apical constriction. Yellow line: ventral midline. Ectoderm cells (magenta dots) still move towards ventral midline even though no ventral furrow was formed (h). The left and right panels in (h) show the mCherry and GFP signals from the same embryo. N = 3 embryos. T = 0 is the onset of apical constriction. All scale bars: 20 μm. **(h)** Cartoon depicting the mechanical bistability of ventral furrow formation. Actomyosin mediated apical constriction is important for the furrow develop into the intermediate state, however, compression helps with the following folding phase, which completes the furrow.

Video Legends

Figure 1 – video 1. Rapid membrane recruitment of CRY2-Rho1DN upon blue light irradiation. Shown is an embryo at late cellularization stage containing CIBNpm-GFP (magenta) and CRY2-Rho1DN-mCherry (green). Stimulation starts when 488-nm laser is turned on at T = 00:00 (mm:ss, same format for all movies). Rapid membrane recruitment of CRY2-Rho1DN-mCherry appears within 10 seconds and maximum recruitment is achieved at around 30 seconds.

Figure 1 – video 2. Loss of apical myosin during apical constriction upon activation of Opto-Rho1DN. Shown is an embryo at early gastrulation stage expressing CIBNpm, CRY2-Rho1DN-mCherry (green) and Sqh-GFP (magenta). Myosin disappears from the apical cortex of the ventral cells within one minute after 488-nm laser illumination.

Figure 4 – video 1. Stage-dependent response to acute myosin inhibition during ventral furrow formation. In Early Group embryos, the apically constricting cells relax immediately as myosin dissociates from the cortex, causing the disappearance of the initial apical indentation. In Mid Group embryos, no obvious relaxation occurs, but ventral furrow invagination is paused for approximately five minutes before invagination resumes. In Late Group embryos, furrow invagination proceeds at a normal speed without obvious pause or tissue relaxation after stimulation. In all cases, apical myosin disappears 60 – 90 sec after stimulation.